Journal of Porous Media

Editor in chief: Prof. K. Vafai, University of California-Riverside, USA.

Impact Factor = 1.752

https://www.begellhouse.com/journals/porous-media.html

Accepted October 21st 2021

EMHD CASSON HYBRID NANOFLUID FLOW OVER AN EXPONENTIALLY ACCELERATED ROTATING POROUS SURFACE

[1]J. Prakash, *[2]Dharmendra Tripathi, [3]O. Anwar Bég and [4]Vineet Srivastava

[1]*Department of Mathematics, Avvaiyar Government College for Women, Karaikal – 609 602,*
U.T of Puducherry, ***India***
[2]*Department of Mathematics, National Institute of Technology Uttarakhand, Srinagar– 246174,* ***India***
[3]*Multi-Physical Engineering, Dept. Mechanical/Aeronautical Engineering, Salford University,*
Manchester, M54WT, ***UK****.*
[4]*Department of Applied Sciences and Humanities, Rajikiya Engineering College, Azamgarh,* ***India.***
Corresponding author: dtripathi@nituk.ac.in

ABSTRACT:

The influence of Coriolis body force, electro-magnetohydrodynamics (EMHD) and thermal radiative heat transfer on the Casson hybrid mixed convection nanofluid driven by an exponentially accelerated plate adjacent to a porous medium in a rotating system is analyzed. Hybrid (Ag- Al_2O_3) and Al_2O_3 nanofluids are considered with ethylene glycol (EG) base fluid. The Maxwell-Garnett model has been deployed to derive the thermal conductivity of the hybrid nanofluid. The electrical potential problem is simplified by applying Debye-Hückel linearization. The Laplace transform method (LTM) is employed to derive closed-form solutions. In terms of heat transfer, the hybrid nanofluid (Ag-Al_2O_3)/EG and nanofluid (Al_2O_3)/EG performance are compared. The benefits of EG-based hybrid nanofluid (Ag-Al_2O_3) relative to EG based (Al_2O_3) nanofluid, are elaborated. The analysis finds applications in centrifugal dynamic electrochromatography under electromagnetic gradient, bio-analytical separation techniques with electric field gradients and rotary bio-inspired DC electromagnetic blood pumps.

Keywords: *Hybrid Ag-Al_2O_3 nanofluids; electro-magneto-hydrodynamics (EMHD); Casson fluid; viscoplastic; radiation heat flux; Laplace transforms; Joule dissipation; rotary blood mixing devices.*

1. INTRODUCTION

Electromagnetic hydrodynamics (EMHD) involves the simultaneous consideration of mutually orthogonal electric and magnetic fields and their interaction with either inviscid or viscous flows. Such flows feature in a range of complex applications in medicine, aerospace, materials processing and increasingly the area of microfluidics. The constitutive equations of EMHD comprise the unification of three sets of field equations: *hydrodynamics equation, electric field equations and magnetic field equations*. While magnetohydrodynamic (MHD) flows [1] concern Lorentzian body force, induction and other effects, electrohydrodynamics (EHD) [2] involves the behavior of bulk charge carriers and invokes electrokinetic phenomena e. g. Debye length effect, electrophoresis etc. When combined the advantages of both may be exploited for optimizing systems. Many excellent studies of such flows have been communicated featuring a variety of theoretical and numerical approaches, as a compliment to experimental works e.g. magnetic field control of liquid metal rotation [3] and variable electrical field manipulation of electroosmotic flow (EOF) in cross straight channel studied with *micro particle image velocimetry (micro-PIV)* [4]. In parallel with these studies many theoretical and numerical investigations of MHD, EHD and also EMHD transport have been reported in recent years in ever widening application. MHD simulations include El-Genk and Paramonov [5] (on nuclear electromagnetic pumps), Tixador [6] (on naval magnetic drive propulsion), Shamshuddin *et al.* [7] (on time-dependent micromorphic coating synthesis), Yang *et al.* [8] (on liquid metal duct processing), Bég *et al.* [9] (seawater MHD generators[10]). EHD analyses include Hollinger and Kennis [11] (electrohydrodynamic-jet (e-jet) printing), Nishihara *et al.* [12] (electrical field control of magnetic hypersonic shock waves), Mandal *et al*. [13](perturbation analysis of leaky dielectric suspended drop rheology under a uniform electric field), Oddy *et al.* [14] (microfluidic bioanalytical applications), Narla *et al*. [15] (bio-inspired pumping of electromagnetic fuels), Meighan *et al.* [16] (dielectrophoresis and electric field gradient focusing in medicine), Bhandari *et al.* [17] (rhythmic propulsion of magnetic fluids). Tripathi *et al.* [18] studied the time-dependent electrokinetic pumping of Newtonian aqueous fluids with a peristaltic mechanism. Tripathi *et al.* [19] examined stratified electro-osmotic blood flow in microchannels using integration methods and Mathematica software. Bianchi [20] deployed variational and penalty finite element methods to simulate the electrokinetic transport in a microscale T-shaped geometry. Ali *et al.* [21] studied axisymmetric two-fluid immiscible peristaltic transport using a forward time centre space finite difference method and perturbation techniques, with applications in diabetic treatment. Hsu *et al.* [22] studied the effect of axial electrical field on electrolytic (blood/plasma) dynamics in an elliptic tube. Further studies of electrohydrodynamic flows include Tripathi *et al.* [23] (on microvascular ionic blood flow), Tsao *et al.* [24] (on electrokinetic viscous flow in an annular gap) and Tripathi *et al.* [25] (on elastic-viscous rhythmic pumping of an ionic fluid in an asymmetric microchannel). Combined electromagnetohydrodynamic (EMHD) flows were studied by Liu *et al.* [26] who considered pulsatile direct current blood pump design featuring dual electrical field and rectilinear reciprocation of the magnet field solenoids with compensation coils. Tripathi *et al.* [27] analysed the pumping under orthogonal electric and magnetic fields of ionic polar liquids in a microchannel. Chakraborty *et al.* [28] computed the effects of Joule dissipation and viscous heating in EMHD heat transfer in slender conduits. Further studies have featured a plethora of Multiphysics including Si and Jian [29] (on viscoelastic rheology in ionic corrugated microchannels), Liu *et al.* [30] (on thermodynamic optimization in curved micro-conduits) and Reddy *et al.* [31] (on electromagnetic instability in stratified channel flows). All these investigations confirmed the considerable impact achieved with electrical and magnetic fields on hydrodynamic characteristics in multiple configurations.

In recent years, a growing trend in biomedical electromagnetic devices and microelectro-mechanical systems (MEMSs) has been the deployment of *rheological working fluent media*. *Non-Newtonian fluid has* feature in many other industrial applications including biochemical mixing, smart coatings and cosmetic materials processing. The Navier-Stokes equations are the fundamental model deployed in fluid dynamics for characterizing Newtonian fluids. However, they are inadequate for describing many different industrial liquids. In the context of non-Newtonian fluids, an extra stress tensor is required, and many robust models have been developed over the past fifty years. These feature different formulations and are applicable for different types of rheological behaviour including stress relaxation, retardation, shear-thinning (pseudoplasticity), shear-thickening (dilatancy), viscoelasticity, viscoplasticity etc. Interesting non-Newtonian models which have been utilized in industrial and biomedical applications include the Jeffrey viscoelastic model [32], Eringen micropolar model [33], Sutterby power-law model [34], Walter-B short memory viscoelastic model [35], Stokes' polar couple stress model [36], the upper convected Maxwell (UCM) model [37], Oldroyd-B model [38], Johnson-Segalman model non-affine viscoelastic model [39], Carreau shear-thinning [40] and Bingham yield stress and Eyring-Powell models [41]. An alternative rheological model that has found substantial popularity in hemodynamics (blood flows) is the Casson model which exhibits yield stress i. e. *viscoplasticity*.

A number of models on the Casson fluid model is developed for biomedical transport [43-45] since it simulates well the simple shear behavior of blood in narrow vessels (130–1000 μm) and also at low shear rates this model predicts yield stress for blood is non-zero. Interesting mathematical models for Casson blood flows have been reported by Khalid *et al.* [46] (with oscillatory effects), Sulochana *et al.* [47] (with thermo-diffusion and radiative heat transfer), Raju *et al.*[48] (on hydromagnetic deformable boundary thermosolutal transport) and Akbar *et al.* [49] (on cilia-generated pumping of Casson liquids under inclined magnetic field with hydrodynamic wall slip and thermal jump).

In recent years thermal enhancement has become a key focus and nanofluids have provided an excellent mechanism for achieving this in many areas of technology including bio-microfluidics, aerospace, environmental and energy systems. Nanofluids [50] are colloidal suspensions engineered at the nanoscale and comprise conventional base fluids e. g. water, doped with metallic (e. g. iron, copper, titanium, gold, silver, zinc and their oxides) or non-metallic (carbon based e. g. silicates, graphene, diamond etc.) nanoparticles (spheres, rods, tubes etc). Following the verification of heat-enhancing properties of nanofluids, many computational studies have appeared exploring the impact of nanoparticles in transport phenomena including Shamshuddin *et al.* [51] (on Marangoni (thermos-capillary) magnetohydrodynamic Cu-water aqueous smart coating of a disk) and Umavathi and Bég [52] (on thermosolutal convection hydrodynamic stability in a couple-stress nanofluid-saturated porous media). Biological and energy applications of nanofluids have been explored by Dubey *et al.* [53] (on nano-pharmacodynamics), Tripathi *et al.* [54] (medical nanofluid based peristaltic pumps with a Buongiorno nanoscale model), Vajravelu *et al.* [55] (thermal coating flows with Ag-water and Cu- water nanofluids) and Kuharat *et al.* [56] (gold water nanofluid direct solar absorber collectors). *Magnetic nanofluids* are another subset of modern nanofluids which feature electrically conducting nanoparticles and invoke magnetohydrodynamic effects, allowing thermal/mass transport to be manipulated. These have been examined by Ramesh et al. [57] (reactive nano-doped convective blood flow), Aneja *et al.* [58] (microorganism-doped nanofluid aqueous functional solar coatings), Fatima *et al.* [59] (COMSOL simulation of laser hyperthermia treatment with superparamagnetic nanoparticles, Basha *et al.* [60] (Keller box numerical computation of high temperature magnetorheological nanofluid coating deposition), Vasu *et al.* [61] (extra-corporeal magnetic field control of stenotic coronary artery nano-drug delivery) *and* Bég et al. [62] (smart orthopaedic magnetic nanofluid films). *Electrohydrodynamic nanofluids* are also another sub-category of functional nanomaterials which respond to external direct or alternating current electric fields. Tripathi et al. [63] were among the earliest researchers to study analytically the electrokinetic pumping of electro-nanofluids with multi-physical effects in microscale conduits. When both properties of electrical and magnetic nanoparticles are combined, the resulting electromagnetohydrodynamic nanofluid offers yet further field-responsive properties. Zhao *et al*. [64] investigated the impact of transverse magnetic and axial electrical fields on EMHD nanofluid dynamics in a microchannel using a Tiwari-Das nanoscale formulation. They showed that both magnetic Hartmann number and electrical body force parameter enhance Nusselt number as does nanoparticle volume fraction. Temperatures were however observed to be depleted with Joule electrical parameter and Brinkman dissipation number. Prakash *et al.* [65] discussed wall thermal jump and radiative flux effects in EMHD bio-inspired propulsion in a microchannel.

Yet another category of nanofluids consisting of combinations of different nanoparticle materials is the *hybrid nanofluid*. It has been observed from both theoretical and experimental studies that hybrid nanofluids achieve even better thermal enhancement characteristics than conventional (unitary i. e. single material) nanofluids. Applications of hybrid nanofluids have been explored in mechanical heat sinks, helical and plate heat exchangers, biocompatible nano-hemodynamics and other areas. A significant difference between hybrid nanofluid and regular nanofluid performance was demonstrated by Rashad et al. [66] who deployed a hybrid mixture of aluminium oxide and copper nanoparticles in triangular enclosure geometries. Lund *et al*. [67] showed that the heat transfer rate in hybrid nanofluids is higher than normal nanofluids. Furthermore, Hayat and Nadeem [68] examined the superior performance of the hybrid mixture compared with unitary nanofluids. Prakash et al. [69] presented the first simulation of hybrid nanofluid electroosmotic pumping slip flow, suing MATLAB bvp4c quadrature for alumina, titania and copper metallic nanoparticle mixtures. They showed that different responses are computed for the different unitary nanofluids with superior thermal performance achieved with all three combined but lower axial pressure gradients for alumina (Al_2O_3) alone, better individual temperature elevation with Cu–water nanoliquid and a stronger temperature increase in selected zones for titania (TiO_2)–water nanoliquid. Other studies have considered combinations of graphite and zinc diamond nanoparticles in hybrid designs. All these studies confirm that improved thermal performance is attained with hybrid nanofluids.

In the current study, motivated by applications in simulating hematological flows in centrifugal devices in presence of electromagnetic fields, a theoretical model is constructed for the collective effects of Coriolis force and EMHD on Casson hybrid nanofluid flow from an exponentially accelerated plate. This novel model combines *MHD, EHD and rotational body force with hybrid nanofluid dynamics and viscoplastic rheology* to produce a more comprehensive representation of actual blood flows in electromagnetic centrifugal devices, which is lacking in the scientific literature. In addition, *radiative heat transfer and porous media* effects are included to generalize the simulations. The flow control equations are first scaled to make them in non-dimensional form and then analytically resolved with the aid of the Laplace transform. Finally, the effects of hybrid nanoparticles, electrical field, rotational effect (Taylor number) on thermofluid characteristics are extensively visualized and elaborated in detail.

2. EMHD BIORHEOLOGICAL ROTATING CONVECTIVE RADIATIVE MODEL

2.1. Flow regime

The regime under consideration is the magnetohydrodynamic-electroosmotic flow of an incompressible hybrid ionic glycol nanofluid in a Darcian saturated porous medium driven by the rotational Coriolis force from an exponentially accelerated plate. The whole system as shown in **Fig. 1** rotates in unison about the $\tilde{y} axis$. Incompressible flow is considered, and the blood is modelled as a Casson viscoplastic aqueous ionic liquid. A transverse magnetic field, B_o, acts in the $\tilde{x}$- direction orthogonally to the electrical field.

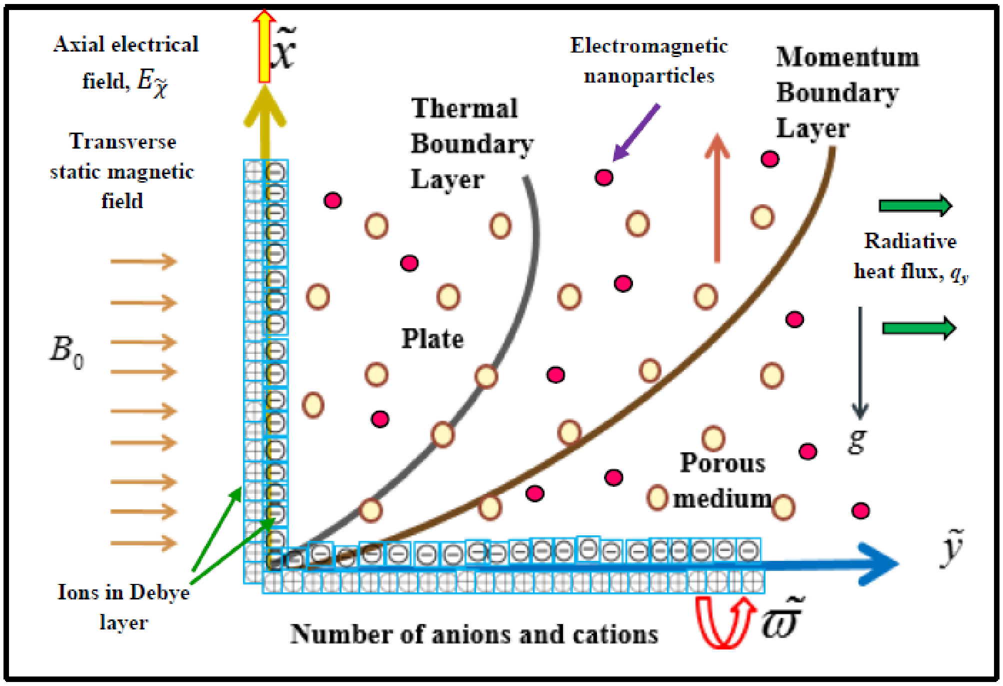

Fig. 1 Geometry of the rotating EHMD hybrid nanofluid problem

The hybrid nanofluid saturates the porous medium (isotropic, homogenous and subject to Darcy's law for viscous-dominated flow). The spherical structure of the two forms of nanoparticles has an average dimension of 25nm, and temperature is 298 *Kalvin* at $\tilde{y}$= 0. The external axial electrical field induces electroosmotic flow, which accelerates the cations entry along the plate. Based on the direction of the applied electrical force, the direction of the ion speed varies. Magnetic Reynolds number is sufficiently small such that magnetic field lines are not distorted, and induction effects are negated. The mathematical problem is articulated by selecting a Cartesian co-ordinate $(\tilde{x}, \tilde{y}, \tilde{z})$ system and the plate lies in the $\tilde{x} - \tilde{y}\ plane,$ with the $\tilde{z}$-axis normal to this plane. At time, $\tilde{t} \leq 0$, both the plate and fluid are at rest and uniform temperature T'_{∞}. At time $\tilde{t} \geq 0$, the plate starts moving in the $\tilde{x}$-direction against the gravitational field with time-dependent velocity $u_0\, cos(\widetilde{a_0}\tilde{t}),$ and the temperature of the plate is raised linearly with time $\tilde{t}$. Assuming that the dominant flow is in the axial $(\tilde{x})$ direction, then all physical quantities may be taken as being functions of $\tilde{y}$ and $\tilde{t}$.

2.2. Governing equations

The hybrid nanofluid is simulated via a volume fraction formulation [66-69]. *Ohm's law determines the influence of the magnetic field.* The linear Darcy law is used to simulate linear bulk matrix impedance of the porous medium. The system is rotated with constant angular speed $\widetilde{\omega}$, and laminar flow is sustained. For the propagation of the electrical potential in the fluid medium, the Poisson-Boltzmann equations are used. Heat generation/absorption is also included. The non-Newtonian characteristics are modelled with the Cauchy stress tensor for a Casson yield stress (viscoplastic) fluid which is defined following [42, 48, 49]:

$$\tau_{ij} = \begin{cases} 2e_{ij}(\mu_B + \frac{Py}{\sqrt{2\pi}})\pi > \pi_c \\ 2e_{ij}(\mu_B + \frac{Py}{\sqrt{2\pi_c}})\pi < \pi_c \end{cases} \tag{1}$$

Here π, μ_B, and Py are the product of the *component of deformation rate, dynamic viscosity, and yield stress of fluid,* $\pi = e_{ij}$ *and*e_{ij} *is the*$(i,j)^{th}$ *element of the deformation rate and* π_c *shows that this product has a non-Newtonian critical value.* The governing equations for the radiative EMHD nanofluid Casson rotating flow can be written as [48, 77, 78]:

Primary momentum

$$\rho_{hnf}\frac{\partial\tilde{u}}{\partial\tilde{t}} = \mu_{hnf}\left(1+\frac{1}{\beta}\right)\frac{\partial^2\tilde{u}}{\partial\tilde{y}^2} - 2\rho_{hnf}\tilde{\omega}\tilde{v} - \sigma_{hnf}B_0^2\tilde{u} - \frac{\mu_{hnf}}{\tilde{k}}\tilde{u} + \tilde{\rho}_e E_{\tilde{\chi}} + g(\rho\gamma)_{hnf}(\tilde{T} - T_\infty), \tag{2}$$

Secondary momentum

$$\rho_{hnf}\frac{\partial\tilde{v}}{\partial\tilde{t}} = \mu_{hnf}\left(1+\frac{1}{\beta}\right)\frac{\partial^2\tilde{v}}{\partial\tilde{y}^2} + 2\rho_{hnf}\tilde{\omega}\tilde{u} - \sigma_{hnf}B_0^2\tilde{v} - \frac{\mu_{hnf}}{\tilde{k}}\tilde{v} + g(\rho\gamma)_{hnf}(\tilde{T} - T_\infty), \tag{3}$$

Energy

$$(\rho C_p)_{hnf}\frac{\partial\tilde{T}}{\partial\tilde{t}} = \kappa_{hnf}\frac{\partial^2\tilde{T}}{\partial\tilde{y}^2} - Q_0(\tilde{T} - T_\infty) - \frac{\partial\tilde{q}_r}{\partial\tilde{y}}. \tag{4}$$

In these partial differential conservation equations, $\tilde{u}$ *and* $\tilde{v}$ *represent the axial and transverse velocity respectively,* $\rho_{hnf}, \mu_{hnf}, \beta, \sigma_{hnf}, \tilde{k}, g, (\rho\gamma)_{hnf}, (\rho C_p)_{hnf}$ *,* κ_{hnf}*,* Q_0 *and* $\tilde{q}_r$ *are the density of hybrid nanofluid, dynamic viscosity, Casson fluid parameter,the electrical conductivity, porosity parameter, acceleration due to gravity, the thermal expansion coefficient of hybrid nanofluid, heat capacitance, the thermal conductivity, heat source/sink rate and radiative heat flux. Also,* $-\sigma_{hnf}B_0^2\tilde{u}$ *denotes the magnetic Lorentzian drag force,* $-\frac{\mu_{hnf}}{\tilde{k}}\tilde{u}$ *is the Darcian porous medium drag force and* $+\tilde{\rho}_e E_{\tilde{\chi}}$ *is the electrokinetic body force in which* $\tilde{\rho}_e$ *is the net charge number density.*

2.3. Radiative heat flux

Rosseland's algebraic approximation' ([51, 60]) is deployed to simulate thermal radiation heat transfer and assumed that the nanofluid-saturated regime is gray, absorbing and emitting but non-scattering for low optical thickness. The appropriate radiative heat flux local gradient is expressed in the following form:

$$\tilde{q}_r = \frac{4\sigma^*}{3k^*}\frac{\partial \tilde{T}^4}{\partial \tilde{y}}, \tag{5}$$

Considering the small temperature differences within the flow, eq.(5) is reduced to

$$\tilde{T}^4 \approx 4T_\infty^3\tilde{T} - 3T_\infty^4, \tag{6}$$

Substituting Eqns. (5) and (6) into (4) we obtain:

$$\frac{\partial \tilde{T}}{\partial \tilde{t}} = \frac{1}{(\rho C_p)_{hnf}}\left(\kappa_{hnf} + \frac{16\sigma^* T_\infty^3}{3k^*}\right)\frac{\partial^2 \tilde{T}}{\partial \tilde{y}^2} - \frac{Q_0(\tilde{T}-T_\infty)}{(\rho C_p)_{hnf}} \tag{7}$$

2.4. Electrical potential

The Poisson equation defines the electrostatic potential produced by the ionic fluid in the regime as:

$$\nabla\tilde{E} = -\frac{\tilde{\rho}_e}{\varepsilon_{eff}}, \tag{8}$$

Here $\varepsilon_{eff} = \varepsilon_0\varepsilon_r$ and $\varepsilon_0$specifies the *relative permittivity of the vacuum* and ε_r is the dielectric constant of the medium. For *symmetric electrolyte solutions*, the charge number density is defined taking electrolyte nanofluid solution with the same valence *z* in the cations and anions:

$$\tilde{\rho}_e = ez(n^+ - n^-), \tag{9}$$

In Eqn. (9) n^- and n^+ are the numbers of anions and cations, with the mass ionic concentration $n_0$and *e* the electronic charge, respectively. Here the potential distribution inside the ionic nanofluid medium can be accurately approximated via the linearized Poisson-Boltzmann distribution. Additionally, the Boltzmann ionic number concentration is computed using:

$$n^{\pm} = e^{\mp\tilde{E}} = e^{\mp\frac{ez\tilde{E}}{k_B T_v}}, \tag{10}$$

Implementing Eqn. (10) in Eqn. (9), we get:

$$\frac{\partial\tilde{E}}{\partial\tilde{y}} = \kappa^2\, sinh\left(\tilde{E}\right) \tag{11}$$

By minimizing the small zeta potentials, which is a viable assumption frequently adopted in electrofluid dynamics, then the Eq.(11) can be linearized as the electrical potential produced by most ionic solutions falls within the range of < 25mV. Noting that $sinh\left(\tilde{E}\right) \approx \tilde{E}$then Eqn. (8) may be readily modified to yield:

$$\frac{\partial\tilde{E}}{\partial\tilde{y}} = \kappa^2\tilde{E} \tag{12}$$

Eqn. (12) is subject to boundary conditions $\tilde{E} = \xi$at $\tilde{y} = 0$ and $\tilde{E} \to 0$ at $\tilde{y} \to \infty$. Furthermore, in Eqn. (12), $K = \frac{vez}{u_0}\sqrt{\frac{2n_0}{\varepsilon_{eff} K_B T_v}} = \frac{(\nu/u_0)}{\lambda_d}$, is known as the electroosmotic parameter or characteristic thickness of the electrical double layer (EDL).

The the correlations for thermophysical properties are given by [66-69]:

$$\rho_{hnf} = (1-\phi_2)\left[(1-\phi_1)\rho_{bf} + \phi_1\rho_{s_1}\right] + \phi_2\rho_{s_2}, \tag{13}$$

$$\left(\rho C_p\right)_{hnf} = (1-\phi_2)\left[(1-\phi_1)\left(\rho C_p\right)_{bf} + \phi_1\left(\rho C_p\right)_{s_1}\right] + \phi_2\left(\rho C_p\right)_{s_2}, \tag{14}$$

$$(\rho\gamma)_{hnf} = (1-\phi_2)\left[(1-\phi_1)(\rho\gamma)_{bf} + \phi_1(\rho\gamma)_{s_1}\right] + \phi_2(\rho\gamma)_{s_2}, \tag{15}$$

$$\kappa_{hnf} = \kappa_{nf}\left(\frac{\kappa_{s_2}+2\kappa_{nf}-2\phi_2\left(\kappa_{nf}-\kappa_{s_2}\right)}{\kappa_{s_2}+2\kappa_{bf}+\phi_1\left(\kappa_{bf}-\kappa_{s_1}\right)}\right), \tag{16}$$

$$\kappa_{nf} = \kappa_{bf}\left(\frac{\kappa_{s_1}+2\kappa_{bf}-2\phi_1\left(\kappa_{bf}-\kappa_{s_1}\right)}{\kappa_{s_1}+2\kappa_{bf}+\phi_1\left(\kappa_{bf}-\kappa_{s_1}\right)}\right), \tag{17}$$

$$\frac{\mu_{hnf}}{\mu_{bf}} = \frac{1}{(1-\phi_1)(1-\phi_2)} = a_1, \tag{18}$$

The electrical conductivity of hybrid nanofluid can be defined as:

$$\frac{\sigma_{hnf}}{\sigma_{bf}} = 1 + \frac{\frac{3(\phi_1\sigma_{s_1}+\phi_2\sigma_{s_2})}{\sigma_{bf}} - 3(\phi_1+\phi_2)}{\left(\frac{(\sigma_{s_1}+\sigma_{s_2})}{\sigma_{bf}}+2\right) - \left(\frac{\sigma_{s_1}\phi_1+\sigma_{s_2}\phi_2}{\sigma_{bf}} - (\phi_1+\phi_2)\right)}. \tag{19}$$

Here the subscript $(\ )_1$ is for Al_2O_3, subscript $(\ )_2$ is for Ag nanoparticles and subscript $(\ )_{bf}$ for base fluid. Further, ϕ_1 and ϕ_2 represent the volume fraction of Al_2O_3 and silver nanoparticles respectively.

2.5. Dimensional boundary conditions

The dimensional boundary conditions are considered as:

$$\tilde{t} = 0: \tilde{u} = 0, \tilde{v} = 0, \tilde{T} = T_\infty \text{ for all } \tilde{y},$$

$$\tilde{t} > 0: \tilde{u} = u_0 \cos(\widetilde{a_0}\tilde{t}), \tilde{v} = 0, \tilde{T} = T_w \text{ at } \tilde{y} = 0,$$

$$\tilde{t} > 0: \tilde{u} \to 0, \tilde{v} \to 0, \tilde{T} \to T_\infty as \tilde{y} \to \infty. \tag{20}$$

Table – 1: Thermo-physical properties of nanoparticles and EG base fluid [66-69]

Physical properties	**Al_2O_3**	**Silver (Ag)**	**Ethylene Glycol (EG)**
Specific heat (C_p) (*J/kg.K*)	765	235	2415
Density ($\boldsymbol{\rho_{hnf}}$) (*kg/m^3*)	3970	10500	1114
Thermal conductivity $\boldsymbol{\kappa_{hnf}}$ (W/mK)	40	429	0.252

Electrical conductivity$\boldsymbol{\sigma_{hnf}}$ (S/m)	3.5 x 10^{7}	6.30 x 10^{7}	5.5 x 10^{-6}
Coefficient of thermal expansion $\boldsymbol{\gamma X 10^{-5} (K^{-1})}$	0.85	1.89	57

2.6 Non-dimensional form of the mathematical model

It is pertinent to invoke the following non-dimensional parameters and variables:

$$y=\frac{\tilde{y}u_0}{v_{bf}},t=\frac{u_0^2\tilde{t}}{v_{bf}},u=\frac{\tilde{u}}{u_0},v=\frac{\tilde{v}}{u_0},\theta=\frac{\tilde{T}-T_\infty}{T_w-T_\infty},k_1=\frac{\tilde{k}u_0^2}{v_{bf}^2},H=\frac{Q_0v_{bf}}{u_0^2\left(\rho C_p\right)_{bf}},Uhs=\frac{-E_{\tilde{\chi}}\varepsilon_{eff}\xi}{\mu_{bf}u_0},$$

$$E=\frac{\tilde{E}}{\xi},G_r=\frac{g\gamma_{bf}v_{bf}(T_w-T_\infty)}{u_0^3},Pr=\frac{\mu_{bf}\beta_{bf}}{\kappa_{bf}},R=\frac{16\sigma^*T_\infty^3}{3k^*\kappa_{bf}},M^2=\frac{B_0^2v_{bf}\sigma_{bf}}{u_0^2\rho_{bf}},\sqrt{Ta}=\frac{v_{bf}\tilde{\omega}}{u_0^2},a_0=\frac{\widetilde{a_0}v_{bf}}{u_0^2}. \tag{21}$$

Implementing Eqn. (21), Eqns. (2)-(4) emerge as follows:

$$\frac{\partial^2 E}{\partial y^2}=K^2E, \tag{22}$$

$$\frac{\partial u}{\partial t}=a_3\left(1+\frac{1}{\beta}\right)\frac{\partial^2 u}{\partial y^2}+Gra_7\theta-\left(M^2a_5+\frac{a_3}{k_1}\right)u-2\sqrt{Ta}v+a_2UhsK^2E, \tag{23}$$

$$\frac{\partial v}{\partial t}=a_3\left(1+\frac{1}{\beta}\right)\frac{\partial^2 v}{\partial y^2}+Gra_7\theta-\left(M^2a_5+\frac{a_3}{k_1}\right)v+2\sqrt{Ta}u, \tag{24}$$

$$\frac{\partial \theta}{\partial t}=a_{12}\frac{\partial^2\theta}{\partial y^2}-\frac{H}{a_8}\theta. \tag{25}$$

Here *u, v,*θ*, Uhs, Gr, k₁, Ta, Pr, R, M, H and* a_0 designate the *axial velocity*(*primary* velocity), transverse (*secondary* velocity), nanoparticle temperature, electroosmotic velocity or Helmholtz Smoluchowski velocity (HS velocity), thermal Grashof number, porous (permeability) parameter, Taylor number, Prandtl number, thermal radiation parameter, magnetic field parameter, heat generation /absorption parameter and frequency parameter. The corresponding boundary conditions are transformed to:

$$\left.\begin{array}{l} t=0: u=0, v=0, \theta=0 \text{ for all } y, \\ t>0: u=cos(\,a_0 t), v=0, \theta=1 \text{ at } y=0, \\ t>0: u\rightarrow 0, v\rightarrow 0, \theta\rightarrow 0 \; as\; y\rightarrow \infty. \\ E=1\; at\; y=0, E\rightarrow 0 y\rightarrow \infty for\; t>0 \end{array}\right\} \tag{26}$$

Eqns. (23) and (24) can be expressed in the following form:

$$\frac{\partial^2 E}{\partial y^2}=K^2 E, \tag{27}$$

$$\frac{\partial F}{\partial t}=a_{14}\frac{\partial^2 F}{\partial y^2}+Gra_7\theta-a_{15}F+a_2UhsK^2E+2i\sqrt{Ta}F \tag{28}$$

$$\frac{\partial \theta}{\partial t}=a_{12}\frac{\partial^2 \theta}{\partial y^2}-\frac{H}{a_8}\theta. \tag{29}$$

Where $F = u+iv$, is a complex variable and a function of both axial (primary) and transverse (secondary) velocity components.

3. ANALYTICAL SOLUTIONS

To obtain exact solutions for ionic nanofluid velocity components and temperature one may solve the Eqs. (27) to (29) subject to Eq. (26) using Laplace transform method (LTM). After simplification the solutions emerge in the following form:

$$E=exp(\,-Ky), \tag{30}$$

The hybrid nanoparticle temperature distribution is derived as:

$$\theta(y,t)=\frac{1}{2}\left[exp(\,y\sqrt{a_{16}a_{13}})erfc(\eta\sqrt{a_{16}}+\sqrt{a_{13}t})+exp(\,-y\sqrt{a_{16}a_{13}})erfc(\eta\sqrt{a_{16}}-\sqrt{a_{13}t})\right], \tag{31}$$

The axial and transverse velocities are combined solutions via the complex variable definition in given earlier, and emerge as:

$$F(y,t)=\frac{exp(\,ia_0t)}{4}\left[\begin{array}{l} exp\left(y\sqrt{(ia_0+a_{17})a_{18}}\right)erfc\left(\eta\sqrt{a_{18}}+\sqrt{(ia_0+a_{17})t}\right) \\ +\,exp\left(-y\sqrt{(ia_0+a_{17})a_{18}}\right)erfc\left(\eta\sqrt{a_{18}}-\sqrt{(ia_0+a_{17})t}\right) \end{array}\right]$$

$$+\frac{exp(-ia_0t)}{4}\begin{bmatrix}exp\left(y\sqrt{(-ia_0+a_{17})a_{18}}\right)erfc\left(\eta\sqrt{a_{18}}+\sqrt{(-ia_0+a_{17})t}\right)\\ +exp\left(-y\sqrt{(-ia_0+a_{17})a_{18}}\right)erfc\left(\eta\sqrt{a_{18}}-\sqrt{(-ia_0+a_{17})t}\right)\end{bmatrix}$$

$$-\frac{a_{26}}{2}\left[exp(\,y\sqrt{a_{17}a_{18}})erfc(\eta\sqrt{a_{18}}+\sqrt{a_{17}t})+exp(\,-y\sqrt{a_{17}a_{18}})erfc(\eta\sqrt{a_{18}}-\sqrt{a_{17}t})\right]$$

$$+\frac{a_{22}\,exp(-a_{21}t)}{2}\begin{bmatrix}exp(\,y\sqrt{a_{18}(a_{17}-a_{21}})erfc(\eta\sqrt{a_{18}}+\sqrt{(a_{17}-a_{21})t})\\ +exp(\,-y\sqrt{a_{18}(a_{17}-a_{21}})erfc(\eta\sqrt{a_{18}}-\sqrt{(a_{17}-a_{21})t})\end{bmatrix}$$

$$+\frac{a_{25}\,exp(-a_{24}t)}{2}\begin{bmatrix}exp(\,y\sqrt{a_{18}(a_{17}-a_{24}})erfc(\eta\sqrt{a_{18}}+\sqrt{(a_{17}-a_{24})t})\\ +exp(\,-y\sqrt{a_{18}(a_{17}-a_{24}})erfc(\eta\sqrt{a_{18}}-\sqrt{(a_{17}-a_{24})t})\end{bmatrix}$$

$$+\frac{a_{22}}{2}\left[exp(\,y\sqrt{a_{16}a_{13}})erfc(\eta\sqrt{a_{16}}+\sqrt{a_{13}t})+exp(\,-y\sqrt{a_{16}a_{13}})erfc(\eta\sqrt{a_{16}}-\sqrt{a_{13}t})\right]$$

$$-\frac{a_{22}\,exp(-a_{21}t)}{2}\begin{bmatrix}exp(\,y\sqrt{a_{16}(a_{13}-a_{21}})erfc(\eta\sqrt{a_{13}}+\sqrt{(a_{13}-a_{21})t})\\ +exp(\,-y\sqrt{a_{16}(a_{13}-a_{21}})erfc(\eta\sqrt{a_{13}}-\sqrt{(a_{13}-a_{21})t})\end{bmatrix}$$

$$+a_{25}\,exp(-Ky)-a_{25}\,exp(-a_{24}t)\,exp(-Ky). \tag{32}$$

In the above expressions, the following notation applies:

$$a_1=\frac{1}{(1-\phi_1)(1-\phi_2)},\,a_2=\frac{1}{(1-\varphi_2)\left[(1-\phi_1)+\frac{\phi_1\rho_{s_1}}{\rho_{bf}}\right]+\frac{\phi_1\rho_{s_2}}{\rho_{bf}}},\,a_3=a_1a_2,$$

$$a_4=1+\frac{\frac{3(\phi_1\sigma_{s_1}+\phi_2\sigma_{s_2})}{\sigma_{bf}}-3(\phi_1+\phi_2)}{\left(\frac{(\sigma_{s_1}+\sigma_{s_2})}{\sigma_{bf}}+2\right)-\left(\frac{\sigma_{s_1}\phi_1+\sigma_{s_2}\phi_2}{\sigma_{bf}}-(\phi_1+\phi_2)\right)},\,a_5=a_4a_2,$$

$$a_6=(1-\phi_2)\left[(1-\phi_1)+\phi_1\frac{(\rho\gamma)_{s_1}}{(\rho\gamma)_{bf}}\right]+\phi_2\frac{(\rho\gamma)_{s_2}}{(\rho\gamma)_{bf}},$$

$$a_7=a_2a_6,\,a_8=(1-\phi_2)\left[(1-\phi_1)+\phi_1\frac{(\rho C_p)_{s_1}}{(\rho C_p)_{bf}}\right]+\phi_2\frac{(\rho C_p)_{s_2}}{(\rho C_p)_{bf}},\,a_9=\left(\frac{\kappa_{s_2}+2\kappa_{nf}-2\phi_2(\kappa_{nf}-\kappa_{s_2})}{\kappa_{s_2}+2\kappa_{bf}+\phi_1(\kappa_{bf}-\kappa_{s_1})}\right),$$

$$a_{10} = \left(\frac{\kappa_{s_1} + 2\kappa_{bf} - 2\phi_1\left(\kappa_{bf} - \kappa_{s_1}\right)}{\kappa_{s_1} + 2\kappa_{bf} + \phi_1\left(\kappa_{bf} - \kappa_{s_1}\right)} \right), a_{11} = a_9 a_{10}, a_{12} = \frac{a_{11} + R}{a_8 \Pr}, a_{13} = \frac{H}{a_8}, \eta = \frac{y}{2\sqrt{t}},$$

$$a_{14} = a_3\left(1 + \frac{1}{\beta}\right), a_{15} = M^2 a_5 + \frac{a_3}{k_1}, a_{16} = \frac{1}{a_{12}}, a_{17} = a_{15} + 2i\sqrt{Ta}, a_{18} = \frac{1}{a_{17}}, a_{19} = a_{14}a_{16},$$

$$a_{20} = \frac{Gra_7}{1 - a_{19}}, \qquad a_{21} = \frac{a_{19}a_{13} - a_{17}}{a_{19} - 1}, a_{22} = \frac{a_{20}}{a_{21}},$$

$$a_{23} = a_2K^2Uhs, a_{23} = a_{17} - a_{14}K^2, a_{25} = \frac{a_{23}}{a_{24}}, a_{26} = a_{22} - a_{25}$$

4. NUMERICAL SOLUTION WITH MATLAB PDEPE FEATUREAND VALIDATION

Since the present model is novel with many new features, it is not possible to benchmark with any comparable studies from the literature. Therefore, a numerical solution is also presented. The system of transient state Eqns. (27)-(29) under boundary conditions (26) are computed with the MATLAB "pdepe" command. The general form of a PDE with initial and boundary value problem with time and a single spatial variable y as

$$\tilde{\mathbb{C}}_i\left(y,t,u,u_y\right) = \frac{\partial}{\partial x}\left(\tilde{\mathbb{Q}}_i\left(y,t,u,u_y\right)\right) + \tilde{\mathbb{N}}_i\left(y,t,u,u_y\right); i = 1,2,3. \tag{34}$$

It is noticed that the function $\tilde{\mathbb{C}}_i, \tilde{\mathbb{Q}}_i \& \tilde{\mathbb{N}}_i, (i = 1,2,3)$can depend on all components of u and u_y with corresponding left and right edge boundary conditions over the stepping distance.

$$\tilde{P}_{li}(y_l,t,u) + \tilde{R}_{li}(y_l,t) * \tilde{B}_{li}\left(y_l,t,u,u_y\right) = 0, (i = 1,2,3). \tag{35}$$

$$\tilde{P}_{ri}(y_r,t,u) + \tilde{R}_{ri}(y_r,t) * \tilde{B}_{ri}\left(y_r,t,u,u_y\right) = 0, (i = 1,2,3). \tag{36}$$

The associated initial conditions:

$$u_i(0,y) = \tilde{f}_i(y), (i = 1,2,3). \tag{37}$$

In the present problem, we have:

$$\tilde{\mathbb{C}} = \begin{pmatrix} 0 \\ 1 \\ 1 \end{pmatrix}; \tilde{\mathbb{Q}} = \begin{pmatrix} 0 \\ a_{14} \\ a_{12} \end{pmatrix}; \tilde{\mathbb{N}} = \begin{pmatrix} 0 \\ G_r a_7 \theta - a_{15} F + a_2 Uhs K^2 E + 2a_2 i\sqrt{Ta} F \\ -a_{13}\theta \end{pmatrix}, \tag{38}$$

The boundary conditions can be written as:

$$\tilde{P}_l = \begin{pmatrix} 1 \\ cos(a_0 t) \\ 1 \end{pmatrix}, \tilde{\mathrm{P}}_r \rightarrow \begin{pmatrix} 0 \\ 0 \\ 0 \end{pmatrix}, \tilde{R} = \begin{pmatrix} 0 \\ 0 \\ 0 \end{pmatrix}, \tag{39}$$

The initial velocity and temperature conditions are:

$$u(0, y) = 0, \theta(0, y) = 0. \tag{40}$$

Then applying Eqns.(37)-(39) in the MATLAB pdepe command. Thereby the numerical solutions are computed for axial and transverse velocities and also the ionic nanoparticle temperature distribution. The Nusselt number i.e. dimensionless heat transfer rate at the plate surface is easily computed based on the gradient of the temperature function. MATLAB comparison with the analytical solution is shown in **Fig. 24** for stationary value of for fixed values of $Pr = 0.71; \phi_1 = 0.05; \phi_2 = 0.15; R = 0.5; t = 0.9; H = 0.5; Uhs = 1; k_1 = 0.5; Ta = 0.3; K = 0.5; a_0 = \frac{\pi}{2}; \beta = 1; M = 0.4$. Excellent correlation is achieved. Confidence in the accuracy of both methods is therefore justifiably very high.

5. COMPUTATIONS AND DISCUSSION

This section provides comprehensive visualization of the graphical solutions for the transport characteristics i.e. primary velocity, secondary velocity and temperature. A comparative study is presented with (Al_2O_3-Ag)/EG hybrid nanofluid (HBN) and (Al_2O_3 / EG) nanofluid. The range of the parameters deployed in all computations is based on earlier numerical studies as well as experimental results – see [50, 61, 66, 69]. The default parameter values are specified as: $\phi_1 =$

$0.05; \phi_2 = 0.15; \beta$=1;$M$=0.4 (weak magnetic field); Gr=1.5 ; (thermal buoyancy exceeds viscous resistance),$R = 0.5; Uhs = 1; a_0 = \pi;$ i.e. weak axial electrical static field and slow rotation, $Pr = 0.71; K = 0.5; H = 0.5; k_1 = 0.5; Ta = 0.3$and $t = 0.45$. **Figs. 2 – 23** have been plotted and physical interpretation of all results is described in due course.

5.1 Flow characteristics

Axial velocity and transverse velocity distributions are illustrated in **Figs. 2 – 19** for the influence of thermal Grashof number (**Figs. 2-3**), magnetic field parameter (**Figs. 4-5**), HS velocity (**Figs. 6-7**), porosity parameter (**Figs. 8-9**), Taylor number (**Figs. 10-11**), Heat generation parameter (**Figs. 12-13**), Casson rheological parameter (**Figs. 14-15**), electroosmosis parameter (**Figs.16-17**) and Al_2O_3 nanoparticle volume fraction (**Figs.18-19**) on the for both illustration of (Al_2O_3-Ag)/EG hybrid nanofluid and (Al_2O_3 / EG) nanofluid. The velocity profiles are compared for both nanofluids and the velocity of (Al_2O_3 / EG) nanofluid is observed to be comparatively higher under the same physical conditions than the velocity of (Al_2O_3-Ag)/EG hybrid nanofluid. Flow deceleration is generally induced with the hybrid nanofluid whereas acceleration is achieved with the unitary nanofluid. Momentum boundary layer thickness is therefore increased for (Al_2O_3-Ag)/EG hybrid nanofluid (HBN) whereas a thinner hydrodynamic boundary layer corresponds to unitary nanofluid ((Al_2O_3 / EG)). However, in both cases the axial (primary) velocity is consistently positive i. e. flow reversal is never induced in the axial velocity field. Conversely there are generally negative values computed for the transverse (secondary) velocity field.

Figs. 2-3, visualizes the evolution in axial and transverse velocities with elevation in thermal Grashof number for both hybrid and unitary nanofluids. The Grashof parameter embodies the relative contribution of thermal buoyancy and viscous force. Elevation in this parameter induces significant intensification in convection currents. This aids momentum development in the boundary layer regime and accelerates the axial flow (Fig. 2) leading to a thinner momentum boundary layer. The acceleration corresponds to enhancement also in ion mobility in the direction of the motion of the accelerated plate (axial). A velocity overshoot is witnessed near the accelerated plate and is progressively displaced further from the plate with increasing Grashof number.

Table – 1: Impact of thermal radiation vs time on *Nusselt number* for fixed value of $\phi_1 = 0.05$; $\phi_2 = 0.15$; *Pr = 0.71 and H = 0.2* for both (Al_2O_3-Ag)/EG hybrid Casson nanofluid and (Al_2O_3 / EG) Casson nanofluid

(Al_2O_3-Ag)/EG hybrid Casson nanofluid				(Al_2O_3 / EG) Casson nanofluid			
R/t	0.3	0.5	0.7	*R/t*			
0.5	0.6091	0.4893	0.4281	0.5	0.7168	0.5756	0.5034
1	0.5513	0.4428	0.3875	1	0.6282	0.5044	0.4411
1.5	0.5073	0.4075	0.3565	1.5	0.566	0.4544	0.3974

Table – 2: Impact of Prandtl number vs time on *Nusselt number* for fixed value of $\phi_1 = 0.05$; $\phi_2 = 0.15$; *R = 0.5 and H = 0.2* for both (Al_2O_3-Ag)/EC hybrid Casson nanofluid and (Al_2O_3 / EG) Casson nanofluid

(Al_2O_3-Ag)/EG hybrid Casson nanofluid				(Al_2O_3 / EG) Casson nanofluid			
Pr/t	0.3	0.5	0.7	*Pr/t*	0.3	0.5	0.7
0.7	0.6091	0.4893	0.4281	0.71	0.7168	0.5756	0.5034
1	0.7229	0.5807	0.5081	1	0.8507	0.6831	0.5974
7	1.9126	1.5363	1.3442	7	2.2508	1.8072	1.5806

Table – 3: Impact of Joule heating parameter vs time on Nusselt number for fixed values of $\phi_1 = 0.05$; $\phi_2 = 0.15$; $R = 0.5$ *and* $Pr = 0.71$ for both (Al_2O_3-Ag)/EC hybrid Casson nanofluid and (Al_2O_3 / EG) Casson nanofluid

(Al_2O_3-Ag)/EG hybrid Casson nanofluid				(Al_2O_3 / EG) Casson nanofluid			
H/t	0.3	0.5	0.7	*H/t*	0.3	0.5	0.7
0.5	0.6594	0.5528	0.5016	0.5	0.7753	0.6494	0.5889
1	0.7401	0.6523	0.6142	1	0.8692	0.7652	0.72
1.5	0.8172	0.7447	0.7164	1.5	0.9588	0.8729	0.8391

Conventional unitary nanofluid generally achieves significantly higher axial velocity magnitudes than the hybrid nanofluid which is damped. For the *forced convection* case, *Gr* = 0, minimum velocity is computed irrespective of the nanofluid considered. Asymptotically smooth profiles are computed for all cases in the free stream confirming the prescription of an adequately large infinity boundary condition in the MATLAB simulations. Fig. 3 shows that transverse (secondary) velocity exhibits a very different response to modification in Grashof number. Transverse velocity is generally negative and is further decreased with elevation in Grashof number i.e. more intense flow reversal in the secondary velocity is induced with stronger thermal buoyancy force. Again, with increasing Grashof number the minima (troughs) are displaced further from the plate surface. In this case the hybrid nanofluid (Al_2O_3-Ag)/EG achieves higher velocities (less negative) than the unitary nanofluid (Al_2O_3 / EG).

Figs. 4-5 illustrate the axial and transverse velocity fields with different values of magnetic field parameter, *M*. The dominant influence of increasing *M* is to damp the primary velocity (Fig. 4).

Higher velocities are again obtained with unitary nanofluid (Al_2O_3 / EG) compared with hybrid nanofluid (Al_2O_3-Ag)/EG and this may be related to the higher density of the latter which inhibits momentum diffusion rate. Clearly in both cases the maximum axial flow acceleration corresponds to the electrically non-conducting nanofluid case (M = 0). The case M = 1 implies an equivalence of transverse Lorentz magnetic drag force and viscous hydrodynamic force, as per the definition of the modified magnetic interaction number, $M^2 = \frac{B_0^2 v_{bf}\sigma_{bf}}{u_0^3\rho_{bf}}$. This is not the classical Hartmann number but instead relates the Lorentz body force, rather than the total magnetic and electric force to the square of the characteristic magnetic field in the system. Although it is a linear impedance force as simulated in the terms, $-(M^2 a_5)u$ and$-(M^2 a_5)v$in the primary momentum Eqn. (23) and the secondary momentum Eqn. (24), it exerts a profound influence on the transport characteristics in magnetohydrodynamics. Although the Lorentzian transverse velocity component is also negative, it exerts a beneficial effect on the secondary velocity (Fig. 5) due to the re-distribution in momentum. The destruction in primary momentum feeds an increment in secondary momentum. Increasing M values therefore accelerate the secondary flow i. e. *transverse velocities becomeless negative*. As earlier, in this case the hybrid nanofluid (Al_2O_3-Ag)/EG consistently achieves higher velocities than the unitary nanofluid (Al_2O_3 / EG) and this may be attributable to the dominant effect of momentum re-distribution which overcomes the nanoparticle density effect in hybrid nanofluid (HBN in the graph). There will also inevitably be an interplay between Lorentzian drag components and also the Coriolis (rotational) body force components which is explained later.

Figs.6-7 depict the response in axial and transverse velocities profiles with elevation in the Helmholtz Smoluchowski (*Uhs*) velocity**.** This is a key parameter in electrokinetics and refers to the maximum electro-osmotic velocity in a system. In electroosmosis this parameter allows an understanding of the degree of movement (mobility) of the bulk solution (ionic nanofluid). Since the diffuse layer is a short distance from the plate surface, therefore the cations inside are mobile, and under the applied voltage, these cations together with their surrounding ionic nanofluid will migrate towards the cathode. Axial velocity of the electroosmotic flow is strongly influenced by the axial electrical field (which appears in the numerator of $Uhs = \frac{-E_{\tilde{\chi}}\varepsilon_{eff}\xi}{\mu_{bf}u_0}$) and negative electrical values correspond to ion mobility in the direction of the accelerated plate. A rise in negative *Uhs* physically means the presence of a larger impeding electric field which depletes axial velocity profile whereas positive *Uhs* accelerates axial flow (assistive electrical field) for both cases of the hybrid and mono nanofluids (Fig. 6). The hybrid nanofluid (Al_2O_3-Ag)/EG attains much higher velocities than the unitary nanofluid (Al_2O_3 / EG) and asymptotically smooth free stream decays are again computed, verifying that the solution range is sufficiently large to capture the true solution in MATLAB. Fig. 7 shows that the opposite effect is computed in the transverse velocity field, *v*; negative *Uhs* increases transverse velocity i. e. it produces *secondary flow acceleration* whereas positive Uhs generates *flow retardation* on the exponentially accelerated plate. Hybrid nanofluid again produces greater transverse velocities than the unitary nanofluid. It is also noteworthy that the cohesive nature of the ionic nanofluid is instrumental in allowing the bulk electrolytic solution to be dragged and this sustains a net flow across the plate surface.

Figs. 8-9 depicts the influence of permeability parameter on axial and transverse velocities profiles for both case of (Al_2O_3-Ag)/EG hybrid nanofluid and (Al_2O_3 / EG) nanofluid. This parameter is defined as $k_1 = \frac{\tilde{k}u_0^2}{v_{bf}^2}$ and arises in the primary and secondary Darcian linear porous drag force components, $-\left(\frac{a_3}{k}\right)u, -\left(\frac{a_3}{k}\right)v,$ which feature in the respective axial and transverse momentum equations (23), (24). Clearly these linear drag forces are inversely proportional to the medium permeability. As k_1

increases the permeability of the medium increases and progressively solid fibers of the porous matrix are depleted. This reduces the Darcian drag force and produces a concomitant acceleration in the primary velocity (Fig. 8) i. e. axial velocity magnitudes are boosted. There is also a progressive displacement of the peak velocity away from the exponentially accelerated plate surface (y=0) with increasing permeability. Of course, in the limit of infinite permeability, all solid fibers will vanish. Positive axial velocities are always sustained indicating that axial flow reversal is never induced. An increase in permeability effect however induces the opposite response in the secondary velocity. There is substantial deceleration (increasingly negative values) computed with increasing permeability (decreasing Darcian impedance). Lower negative values again correspond to the (Al_2O_3-Ag)/EG hybrid nanofluid compared with (Al_2O_3 / EG) unitary nanofluid.

Figs.10-11. visualize the impact of modification in Taylor number $\left(Ta = \left(\frac{v_{bf}\Omega}{u_0^2}\right)^2\right)$on axial velocity and transverse velocity distributions. Taylor number embodies the ratio of Coriolis (rotational) and viscous force and the definition here uses the initial velocity of the exponential accelerated plate. As the Taylor number increases, the Coriolis force is boosted, which inhibits the momentum development. Ta appears in the primary and secondary Coriolis body forces, viz$-2a_2\sqrt{Ta}v$ and $+2a_2\sqrt{Ta}u$ appearing in the respective momenta equations (23, 24). However, unlike Lorentzian magnetic drag and Darcian drag forces, the primary momentum equation Coriolis body forces features the secondary velocity and vice versa for the secondary momentum equation Coriolis body forces. There is therefore a cross-play between these body forces and with greater Taylor number both axial (primary) and transverse (secondary) velocity fields are strongly damped. Marked primary and secondary flow deceleration is therefore induced with greater Taylor numbers and the maximum velocity magnitudes correspond to the non-rotating scenario (Ta = 0). Rotation therefore offers a very potent regulatory mechanism for controlling the electromagnetohydrodynamic flow from the accelerating plate and is infact equally as influential as the magnetic damping and Darcian drag effect, although it induces the same response in both primary and secondary velocities, whereas these other two effects produce different responses in the different velocities. However, a key similarity again is that the primary flow is greater for (Al_2O_3 / EG) unitary nanofluid compared with (Al_2O_3-Ag)/EG hybrid nanofluid, whereas the secondary velocities are higher for (Al_2O_3-Ag)/EG hybrid nanofluid relative to and (Al_2O_3 / EG) nanofluid.

Figs.12- 13 visualize the impact of (heat generation parameter) H on u and v again for both(Al_2O_3-Ag)/EG hybrid nanofluid and (Al_2O_3 / EG) nanofluid. It is evident that the highest heat absorption produces the least axial velocity (Fig. 12) for both hybrid nanofluid and unitary nanofluid. In the absence of heat generation ($H = 0$) maximum axial velocity is computed for both the hybrid and unitary nanofluid. The (Al_2O_3-Ag)/EG hybrid nanofluid again attains lower axial velocity magnitudes relative to the (Al_2O_3 / EG) nanofluid. Fig. 13 shows that again the opposite behaviour is induced in the secondary flow. Increasing heat generation effect clearly elevates the secondary (transverse) velocity i. e. values become less negative. In this case as in other graphs, (Al_2O_3-Ag)/EG hybrid nanofluid produces better secondary flow acceleration than the unitary (Al_2O_3 / EG) nanofluid. Of course, the case of a heat sink ($H<0$) in which heat is removed from the accelerated plate rotating electro osmotic magnetized boundary layer regime may also be investigated but has been omitted here.

Figs.14-15 visualize the influence of Casson rheological fluid parameter (β) on axial velocity and transverse velocity distributions for both hybrid nanofluid and unitary nanofluid. This parameter characterizes the viscoplastic nature of the ionic nanofluids considered. It features in the augmented shear terms in both momentum equations (23), (24), viz: $a_3\left(1+\frac{1}{\beta}\right)\frac{\partial^2 u}{\partial y^2}$, $a_3\left(1+\frac{1}{\beta}\right)$ $\frac{\partial^2 v}{\partial y^2}$. It is evidently a *reciprocal parameter*. Increasing (β) will elevate the viscosity of the nanofluid and *inhibit momentum diffusion*. This manifests in a reduction in axial velocity reduces with enhanced value of Casson fluid parameter and an associated thickening of the momentum boundary layer. The case of Newtonian ionic nanofluid is retrieved for $\beta = 0$, and evidently maximum axial flow acceleration is achieved with this scenario for both hybrid and unitary nanofluids. Secondary flow is conversely accelerated with increasing Casson parameter, unlike the primary flow which is markedly damped. The destruction in primary momentum on the rotating plate is compensated by a boost in secondary momentum which leads to a rise in transverse velocity values. Whereas the primary flow is maximized for unitary nanofluid, the secondary flow is greater for hybrid nanofluid.

Figs.16-17 depicts the evolution in axial velocity and transverse velocity with a change in electroosmosis parameter for both nanofluids. It is evident from Fig. 16 that there is a significant improvement in the axial velocity with increment in the length of Debye parameter for both nanofluids. $K = \frac{vez}{u_0}\sqrt{\frac{2n_0}{\varepsilon K_B T_v}} = \frac{(\nu/u_0)}{\lambda_d}$, represents the electrical double layer (EDL) parameter and $K \propto 1/\lambda_d$ *where* λ_d is the *EDL thickness* for *fixed* kinematic viscosity (ν) and plate acceleration velocity (u_0), a growth in K relates to a thinner EDL for both hybrid nanofluid and unitary nanofluid. The electric potential improves for dilute ionic nanofluids which mobilizes acceleration in the ion transport. This assists in momentum development and induces primary (axial) flow acceleration. However, in Fig.17, increasing K values manifest in a strong transversal (secondary) flow deceleration since transverse velocity decreases (values become more negative) with increased values of electroosmosis parameter for both case of (Al_2O_3-Ag)/EG hybrid nanofluid and (Al_2O_3 / EG) nanofluid. Therefore, an increment in the inverse Debye length parameter (K) induces strong primary flow acceleration (thinner momentum boundary layer) whereas it produces significant damping in the secondary flow (thicker hydrodynamic boundary layer thickness). The case of non-electrical flow is retrieved for $K = 0$ wherein ionic mobility is negated and the Debye length vanishes.

The effect of the nanoparticle volume fraction on axial velocity and transverse velocity are depicted in **Figs.18-19.** Fig. 18 indicates that a substantial drop in the axial velocity *(primary flow retardation)* is induced in the unitary nanofluid when it is doped with large volume fractions of Al_2O_3 nanoparticles. The agglomeration effect is increased and owing to larger ballistic collisions with higher percentages of nanoparticles in the unitary nanofluid, primary momentum is destroyed, and axial velocity is reduced. However, for the case of the hybrid nanofluid, the influence is much less dramatic. A slight damping effect is produced with higher volume fraction ($\phi 1$) near the plate surface; this trend is reversed further from the wall deeper into the boundary layer and a notable acceleration then accompanies the primary flow into the free stream. The dual effect may be associated with clustering of nanoparticles near the wall and the subsequent homogenous spacing in these nanoparticles further from the boundary which assists in primary flow acceleration in the hybrid nanofluid. A more consistent response is observed in the secondary (transverse) velocity (Fig.19) where significant acceleration is induced with increasing volume fraction at all locations from the plate surface for both unitary and hybrid nanofluids.

5.2 Nanoparticles temperature distributions

The influence of Prandtl number (Fig.20), time parameter (Fig.21), thermal radiation (Fig.22) and Joule heating parameter (Fig.23) on the nano-particle temperature distributions (θ) are visualized in **Figs. 20-23** for both cases of (Al_2O_3-Ag)/EG hybrid nanofluid and (Al_2O_3 / EG) nanofluid.

Fig. 20 below indicates that elevation in Prandtl (*Pr*) contributes to a reduction in temperature profiles for both nanofluids. This is due to a comparatively limited thermal conductance of a fluid with a high Prandtl numbers that lowers the thermal boundary layer thickness. Aqueous ionic nanofluids correspond to higher Prandtl number (Pr =7.0). Prandtl number defines the ratio of momentum diffusion rate to the thermal diffusion rate. It also quantifies the relative thicknesses of the momentum (hydrodynamic) and thermal boundary layer thicknesses. When Pr = 1.0 these two diffusion rates (and boundary layer thicknesses are equal). For Pr < 1 thermal diffusion dominates momentum diffusion, and this explains the higher temperatures for Pr = 0.7. For Pr > 1 momentum diffusion dominates thermal diffusion and leads to a depletion in temperatures. Temperature cays very quickly from the plate surface to the free stream and smooth convergence of solutions is sustained at all Prandtl numbers. Hybrid nanofluid consistently produces much higher temperatures than unitary nanofluid and this is the principal motivation for using combinations of metallic nanoparticles i.e. thermal enhancement. **Fig.21** shows that with progressive elapse in time (*t*), for both (Al_2O_3-Ag)/EG hybrid nanofluid and (Al_2O_3/EG) nanofluid, there is a sustained elevation in temperatures at all locations in the boundary layer. With greater time, the ionic nanofluid has greater ability to diffuse heat i. e. energy distribution is boosted. Ballistic collisions between nanoparticles are also proliferated and these also contribute to the generation of heat in the bulk ionic fluid. The regime is therefore strongly heated (thicker thermal boundary layer) and once again hybrid nanofluid achieves the best thermal performance. It is also noteworthy that while the influence of Grashof number on temperature profiles is not explicitly illustrated, it will also influence the temperature field via coupling with the buoyancy force terms $+G_r a_3 \theta$ and $+G_r a_7 \theta$ featuring in the primary (axial) and secondary (transverse) momentum boundary layer equations (23, 24), respectively. Temperatures will be reduced however for both nanofluids.

Fig. 22 shows that an increase in thermal radiation parameter (R) for both hybrid nanofluid and mono nanofluid strongly energizes the ionic nanofluid regime and enhances temperatures irrespective of the location along the transverse direction. The thermal conduction term is augmented with greater radiative heat transfer and thermal diffusion in the nanofluid is encouraged. Thermal boundary layer thickness is also elevated. The case of $R = 0$ corresponds to conductive-convective heat transfer in the regime for which radiative effects are negated and therefore minimal temperature values are computed in the regime. The inclusion of radiation is important in medical applications e. g. thermal ablative therapy in tissue repair and perfused blood devices. **Fig. 23** above reveals that with greater decrease in the temperature profiles of the Heating Parameter (H) for both hybrid nanofluid and unitary nanofluid. Higher values of Joule heating parameter (H) reduce the thermal diffusion in the regime and raise the surface temperature gradient (at the plate) for both hybrid nanofluid and unitary nanofluid. Finally, it is observed that the hybrid nanofluid again produces much higher temperatures compared with unitary nanofluid at all locations along the accelerated plate in the transverse direction (y)and the efficacy of utilizing hybrid metallic nanoparticle combinations in a single base fluid is again verified.

5.3 Nusselt number distributions

Nusselt number provides an estimate of the heat transfer rate to the plate surface from the bulk nanofluid. It also quantifies the relative role of thermal convection to thermal conduction in the regime. The influence of thermal radiation, Prandtl number and Joule heating parameter are presented in **Tables 1-3** for both case of (Al_2O_3-Ag)/EG hybrid nanofluid and (Al_2O_3 / EG) nanofluid. Table-1 shows the Nusselt number for different values of *R* for both nanofluids. It is observed that Nusselt number decreases with increment in *R*, *since greater radiative flux boosts temperatures within the bulk nanofluid and this will deplete the rate of heat transfer to the plate boundary.* Table - 2 displays the effect of *Pr* on Nusselt number for both hybrid nanofluid and mono nanofluid and noted that Nusselt number upturns with rising *Pr* since temperatures in the bulk ionic nanofluid are depressed (see earlier graphs) and this manifests in a boost in heat transferred to the boundary (plate). However, with progression in time, Nusselt numbers are depressed (again this is due to the elevation in temperatures in the bulk fluid computed earlier which draws heat away from the plate). **Table - 3** shows the influence of Joule heating parameter on Nusselt number for both case of (Al_2O_3-Ag)/EG hybrid nanofluid and (Al_2O_3 / EG) nanofluid. Noted that Nusselt number enhances with enhancing the Joule heating, again in consistency with the depression in temperatures computed in earlier graphs.

6. CONCLUSIONS

Numerical solutions are obtained with the MATLAB pdepe solver achieving excellent agreement with the analytical solutions. The principal outcomes of the current analysis may be précised as follows:

- Increasing Taylor number (i. e. greater Coriolis force relative to viscous force) suppresses both velocity values for both nanofluids, although unitary nanofluid achieves improved acceleration relative to hybrid nanofluid.
- Increasing thermal Grashof number, electroosmosis parameter and Helmholtz Smoluchowski (HS) velocity accelerates the primary flow, whereas it damps the secondary flow, for both hybrid nanofluid and mono nanofluid.

- An elevation in magnetic field parameter reduces axial velocity whereas it enhances transverse velocity for both nanofluids; hybrid nanofluid (Al_2O_3-Ag)/EG consistently achieves higher velocities than the unitary nanofluid (Al_2O_3 / EG).
- With increment in Casson viscoelastic parameter, amplitude of the axial velocity is decreased (primary flow retardation) whereas the transverse velocity is elevated (secondary flow acceleration). The results of the viscous nanofluid model can be easily recovered for $\beta \to \infty$.
- Nanoparticle temperatures are reduced with increasing value of Prandtl number and Joule heating parameter for both (Al_2O_3-Ag)/EG hybrid nanofluid and (Al_2O_3 / EG) nanofluid.
- Nusselt number is reduced for (Al_2O_3-Ag)/EG hybrid nanofluid relative to (Al_2O_3 / EG) nanofluid, since higher temperatures are produced in the ionic nanofluid for the former, confirming the beneficial properties of hybrid metallic nanoparticles in EMHD biomedical flows.
- Increasing permeability parameter i. e. weaker Darcian bulk matrix impedance generates strong primary flow acceleration but transversal (secondary) flow deceleration.

The present study has furnished some useful insights into rotating EMHD nanofluid dynamics of relevance to for example medical hemotological centrifugal biomagnetic devices. However magnetic induction and also Taylor hydrodynamic dispersion effects have been ignored. These may be considered in future studies in addition to alternative non-Newtonian models.

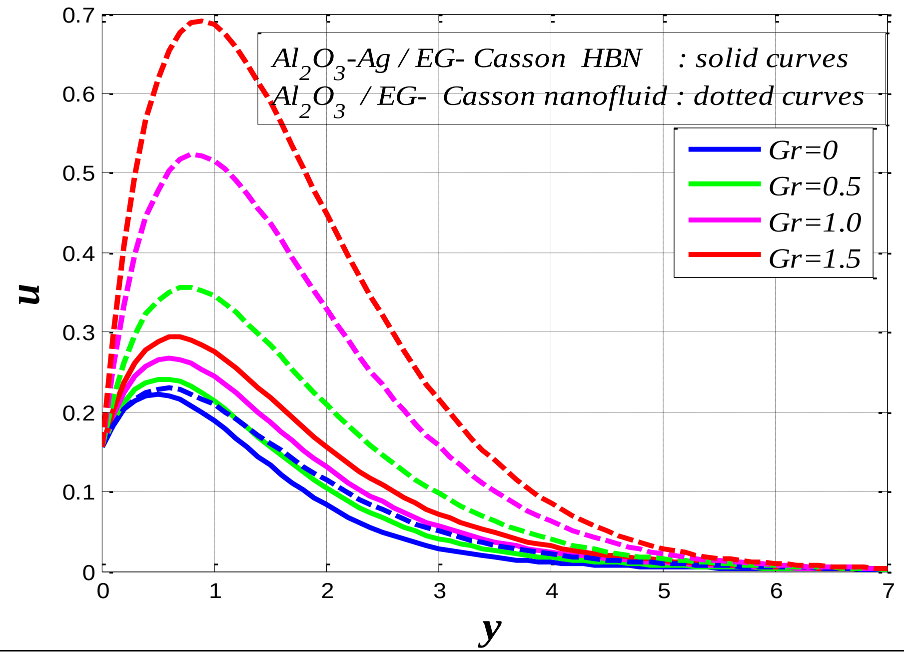

Fig. 2 Variation in axial velocity with thermal Grashof number for fixed values of $Pr = 0.71;\ \phi_1 = 0.05;\ \phi_2 = 0.15; R = 0.5; t = 0.9; H = 0.5; Uhs = 1; k_1 = 0.5; Ta = 0.3; K = 0.5; a_0 = \frac{\pi}{2}; \beta = 1; M = 0.4$.

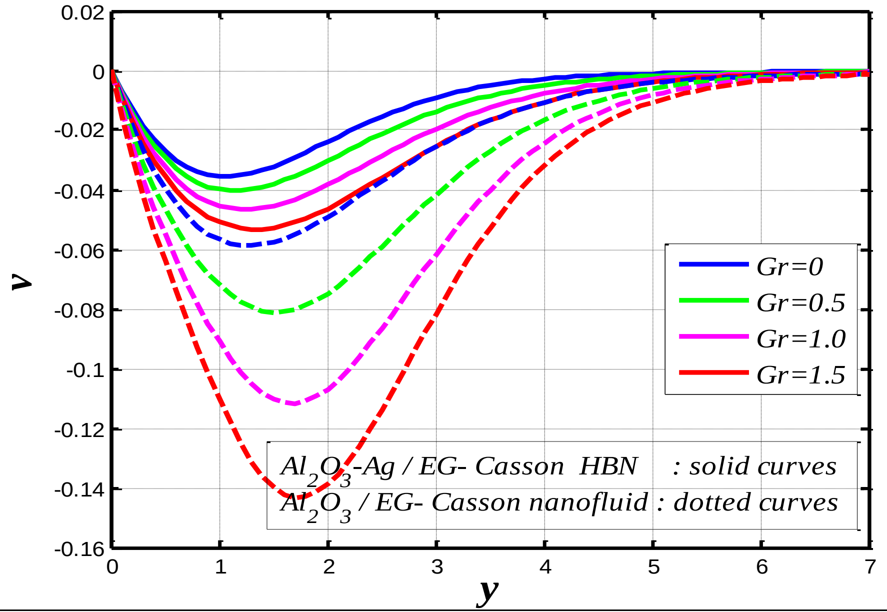

Fig. 3 Variation in transverse velocity with thermal Grashof number for fixed values of $Pr = 0.71;\ \phi_1 = 0.05;\ \phi_2 = 0.15; R = 0.5; t = 0.9; H = 0.5; Uhs = 1; k_1 = 0.5; Ta = 0.3; K = 0.5; a_0 = \frac{\pi}{2}; \beta = 1; M = 0.4$.

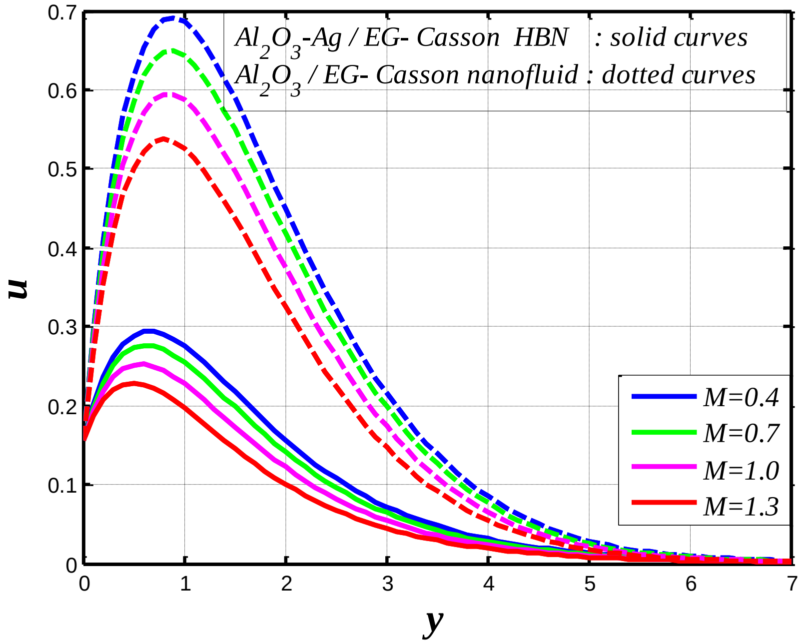

Fig. 4 Effects of magnetic field interaction parameter on axial velocity for fixed values of $Pr = 0.71;\ \phi_1 = 0.05;\ \phi_2 = 0.15; R = 0.5; t = 0.9; H = 0.5; Uhs = 1; k_1 = 0.5; Ta = 0.3; K = 0.5; a_0 = \frac{\pi}{2}; \beta = 1; Gr = 1.5$.

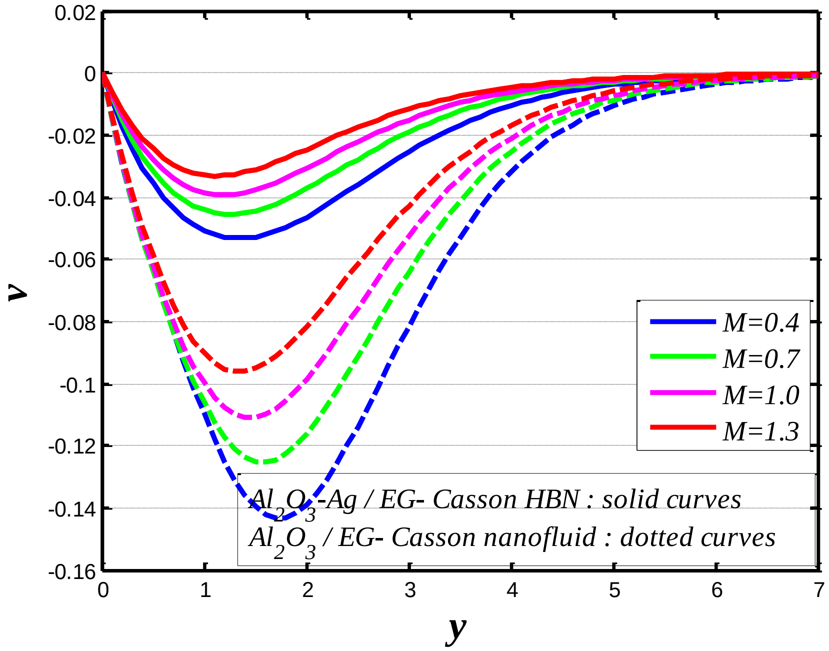

Fig. 5 Effects of magnetic field interaction parameter on transverse velocity for fixed values of $Pr = 0.71;\ \phi_1 = 0.05;\ \phi_2 = 0.15; R = 0.5; t = 0.9; H = 0.5; Uhs = 1; k_1 = 0.5; Ta = 0.3; K = 0.5;\ a_0 = \frac{\pi}{2}; \beta = 1; Gr = 1.5$.

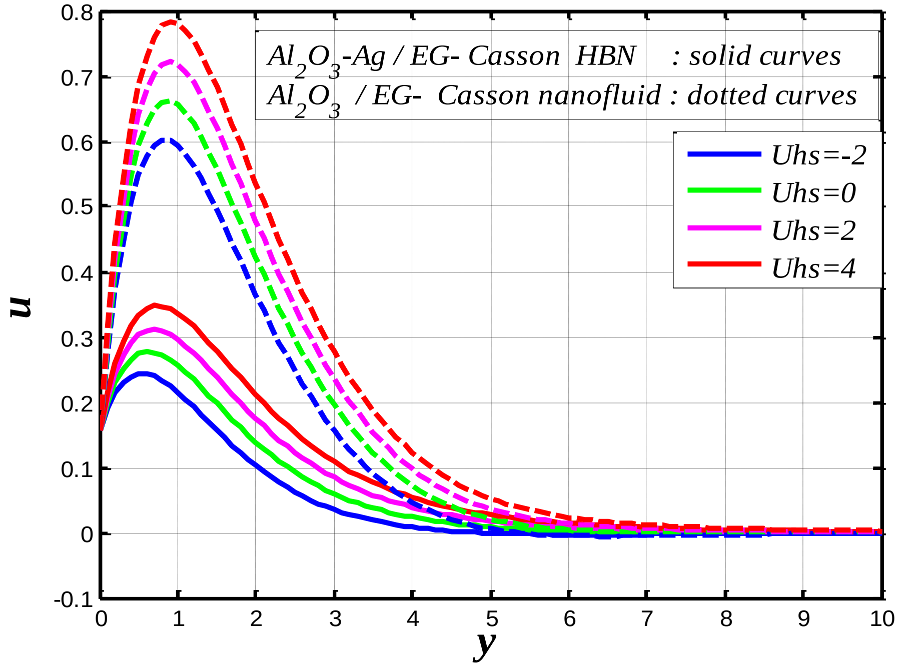

Fig. 6 Impact of *Uhs* on axial velocity for fixed values of $Pr = 0.71;\ \phi_1 = 0.05;\ \phi_2 = 0.15; R = 0.5; t = 0.9; H = 0.5; M = 1; k_1 = 0.5; Ta = 0.3; K =\ 0.5;\ a_0 = \frac{\pi}{2}; \beta = 1; Gr = 1.5$.

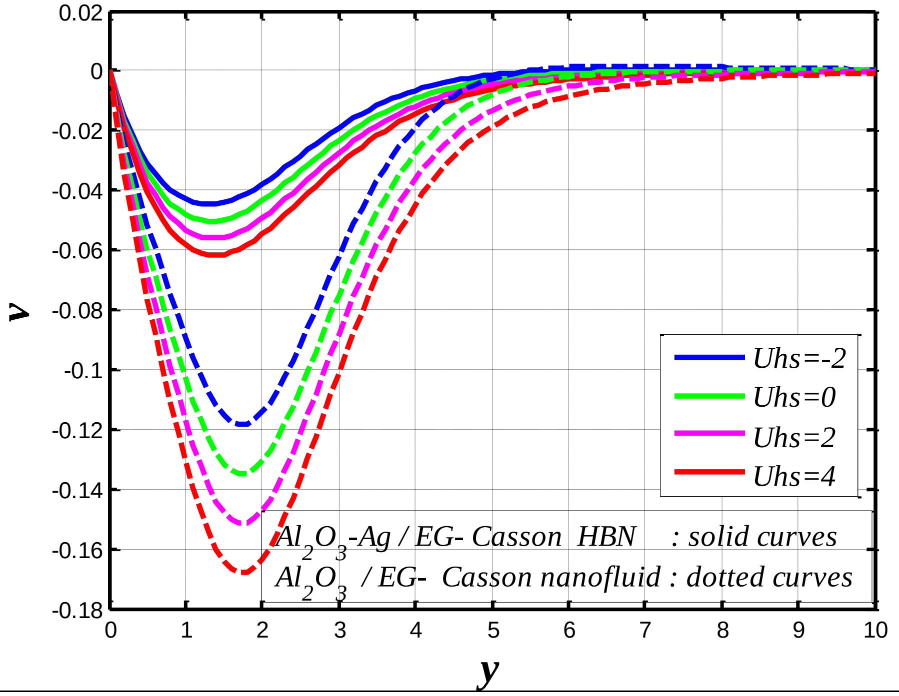

Fig. 7 Impact of Uhs on transverse velocity for fixed values of $Pr = 0.71$; $\phi_1 = 0.05$; $\phi_2 = 0.15$; $R = 0.5$; $t = 0.9$; $H = 0.5$; $M = 1$; $k_1 = 0.5$; $Ta = 0.3$; $K = 0.5$; $a_0 = \frac{\pi}{2}$; $\beta = 1$; $Gr = 1.5$.

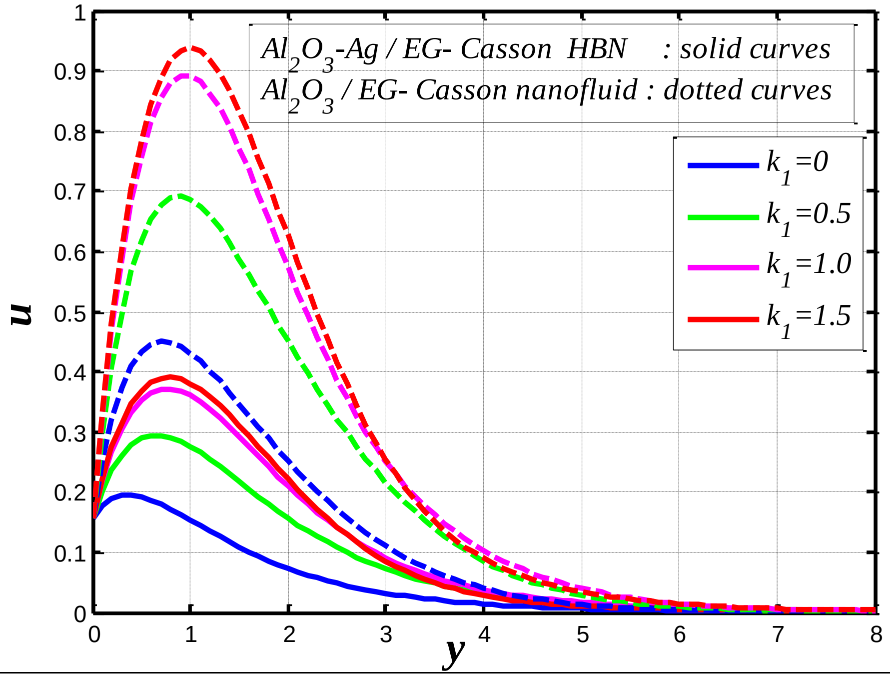

Fig. 8 Impact of k_1 on axial velocity for fixed values of $Pr = 0.71$; $\phi_1 = 0.05$; $\phi_2 = 0.15$; $R = 0.5$; $t = 0.9$; $H = 0.5$; $Uhs = 1$; $M = 0.4$; $Ta = 0.3$; $K = 0.5$; $a_0 = \frac{\pi}{2}$; $\beta = 1$; $Gr = 1.5$.

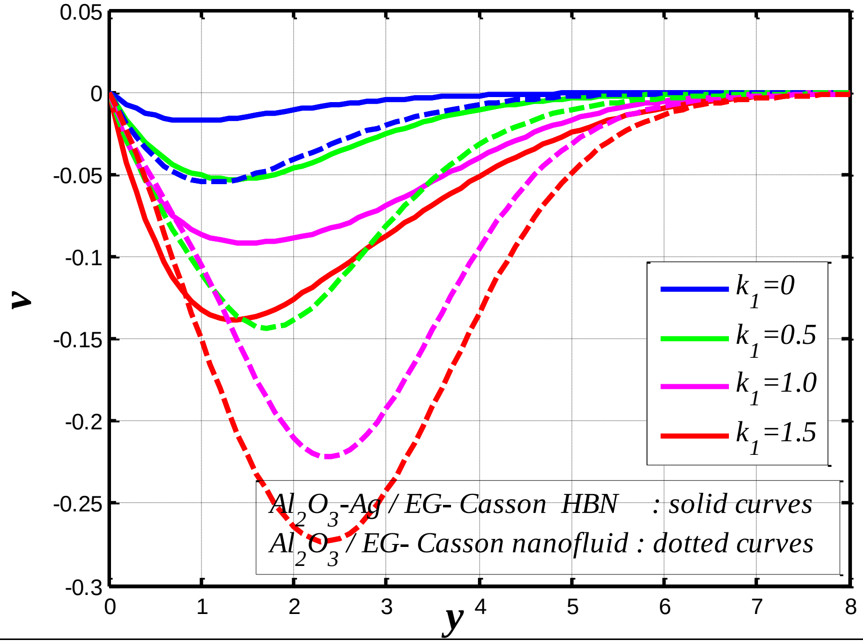

Fig. 9 Impact of k_1 on transverse velocity for fixed values of $Pr = 0.71;\ \phi_1 = 0.05;\ \phi_2 = 0.15; R = 0.5; t = 0.9; H = 0.5; Uhs = 1; M = 0.4; Ta = 0.3; K = 0.5;\ a_0 = \frac{\pi}{2}; \beta = 1; Gr = 1.5$.

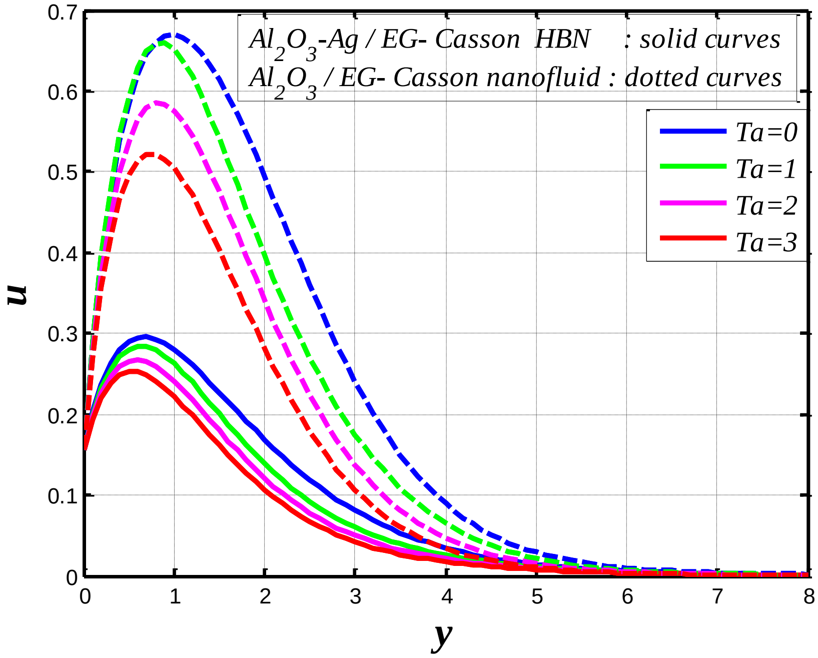

Fig. 10 Impact of Taylor number on axial velocity for fixed values of $Pr = 0.71;\ \phi_1 = 0.05;\ \phi_2 = 0.15; R = 0.5; t = 0.9; H = 0.5; Uhs = 1; k_1 = 0.5; M = 0.4; K = 0.5;\ a_0 = \frac{\pi}{2}; \beta = 1; Gr = 1.5$.

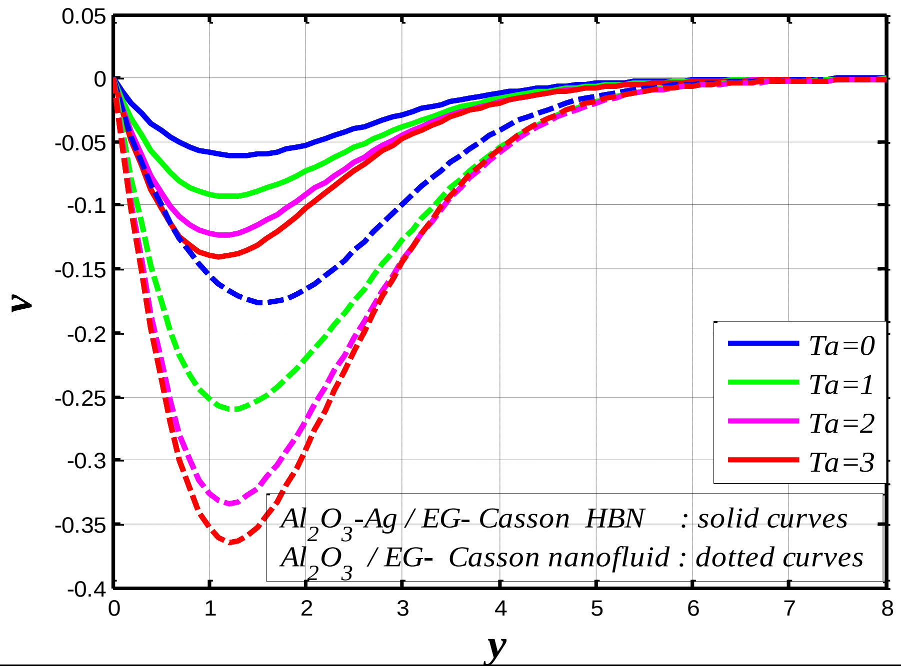

Fig. 11 Impact of Taylor number on transverse velocity for fixed values of $Pr = 0.71;\ \phi_1 = 0.05;\ \phi_2 = 0.15; R = 0.5; t = 0.9; H = 0.5; Uhs = 1; k_1 = 0.5; M = 0.4; K = 0.5;\ a_0 = \frac{\pi}{2}; \beta = 1; Gr = 1.5$.

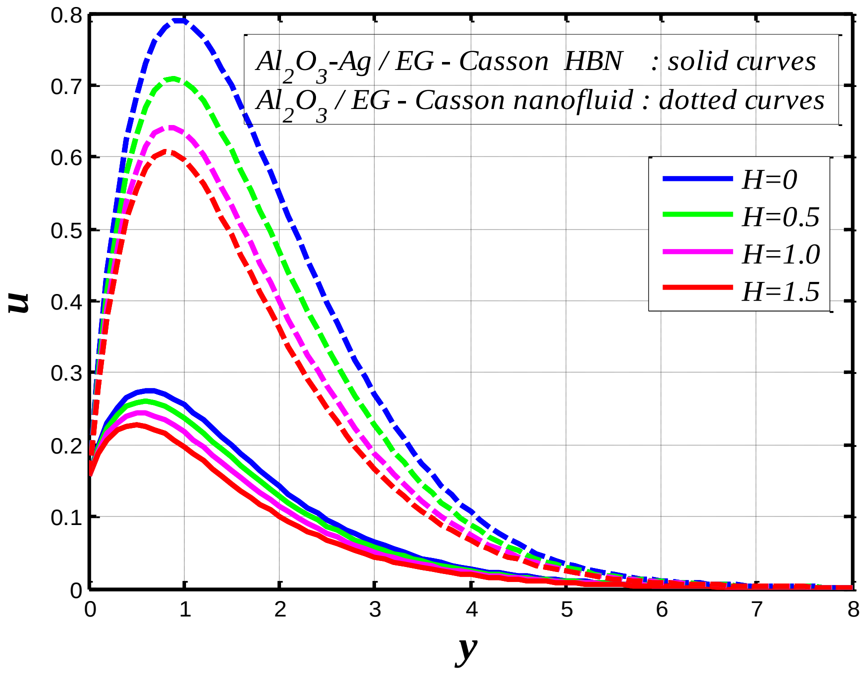

Fig. 12 Impact of heat generationparameter on axial velocity for fixed values of $Pr = 0.71;\ \phi_1 = 0.05;\ \phi_2 = 0.15; R = 0.5; t = 0.9; M = 0.7; Uhs = 1; k_1 = 0.5; Ta = 0.3; K = 0.5;\ a_0 = \frac{\pi}{2}; \beta = 1; Gr = 1.5$.

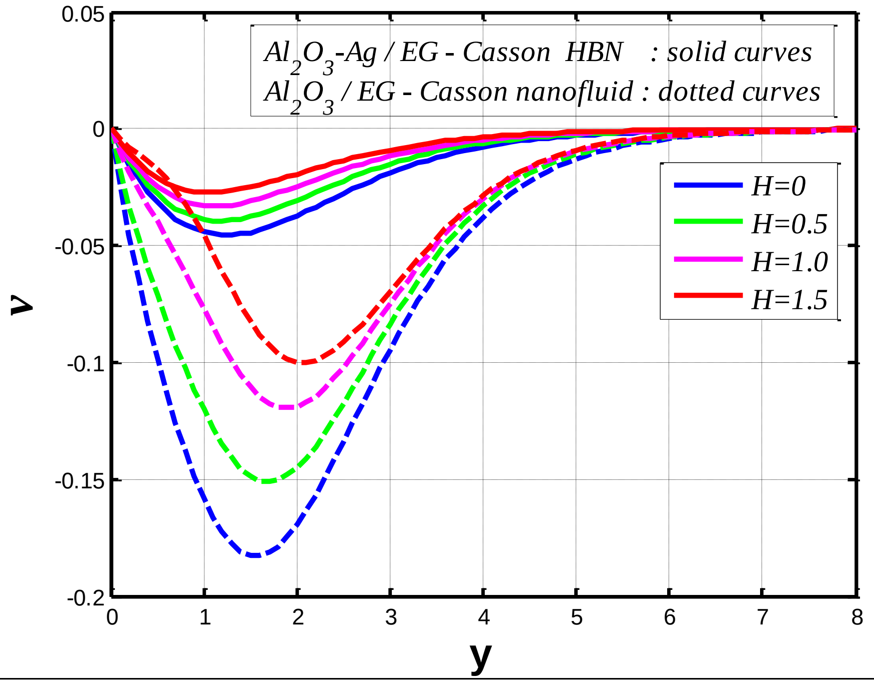

Fig. 13 Impact of heat generationparameter on transverse for fixed values of $Pr = 0.71;\ \phi_1 = 0.05;\ \phi_2 = 0.15; R = 0.5; t = 0.9; M = 0.7; Uhs = 1; k_1 = 0.5; Ta = 0.3; K = 0.5;\ a_0 = \frac{\pi}{2}; \beta = 1; Gr = 1.5$.

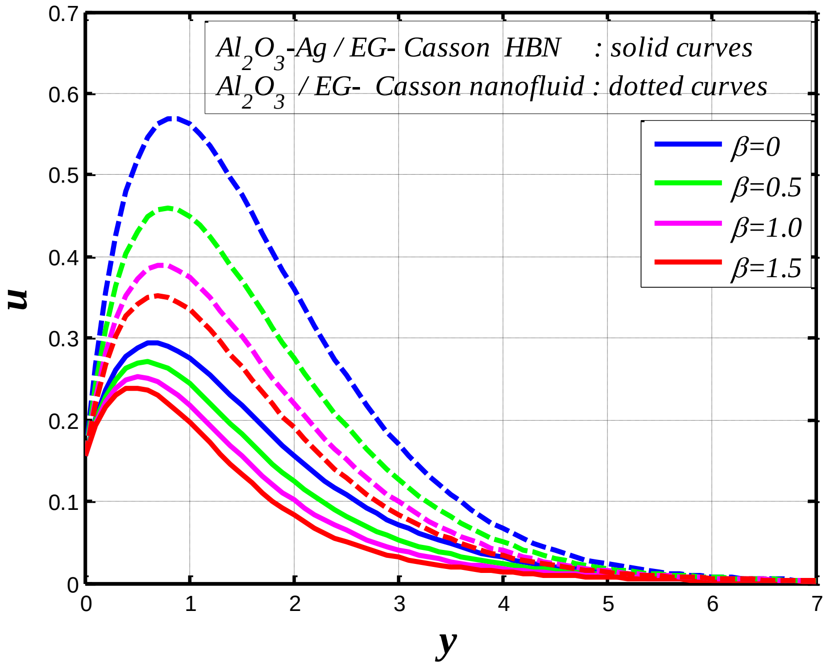

Fig. 14 Effect of rheological parameter on axial velocity for fixed values of $Pr = 0.71;\ \phi_1 = 0.05;\ \phi_2 = 0.15; R = 0.5; t = 0.9; H = 0.5; Uhs = 1; k_1 = 0.5; Ta = 0.3; K = 0.5;\ a_0 = \frac{\pi}{2}; M = 0.4;\ Gr = 1.5$.

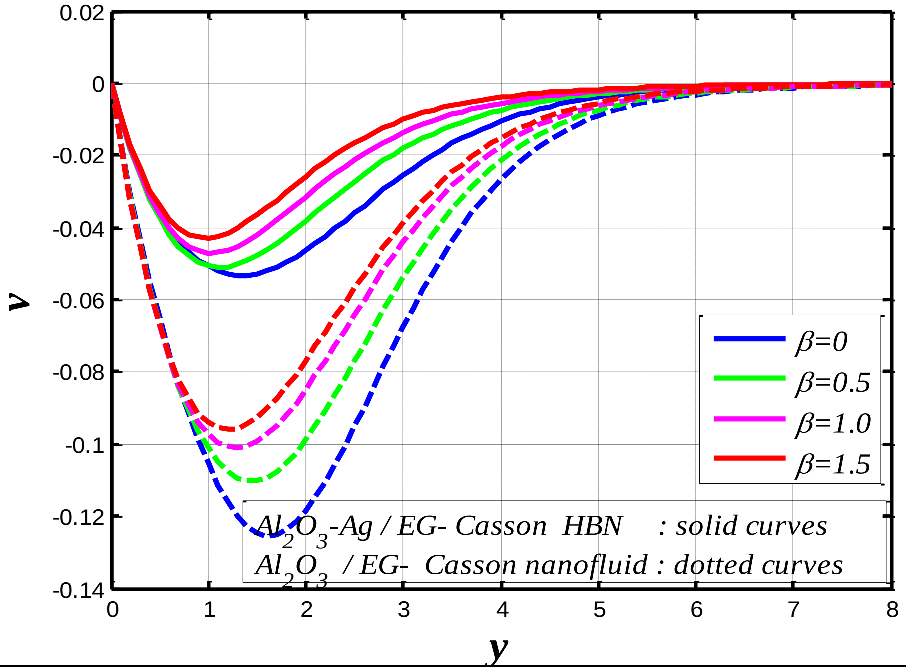

Fig. 15 Effect of Casson rheological parameter on transverse velocity for fixed values of $Pr = 0.71;\ \phi_1 = 0.05;\ \phi_2 = 0.15; R = 0.5; t = 0.9; H = 0.5; Uhs = 1; k_1 = 0.5; Ta = 0.3; K = 0.5;\ a_0 = \frac{\pi}{2}; M = 0.4;\ Gr = 1.5$.

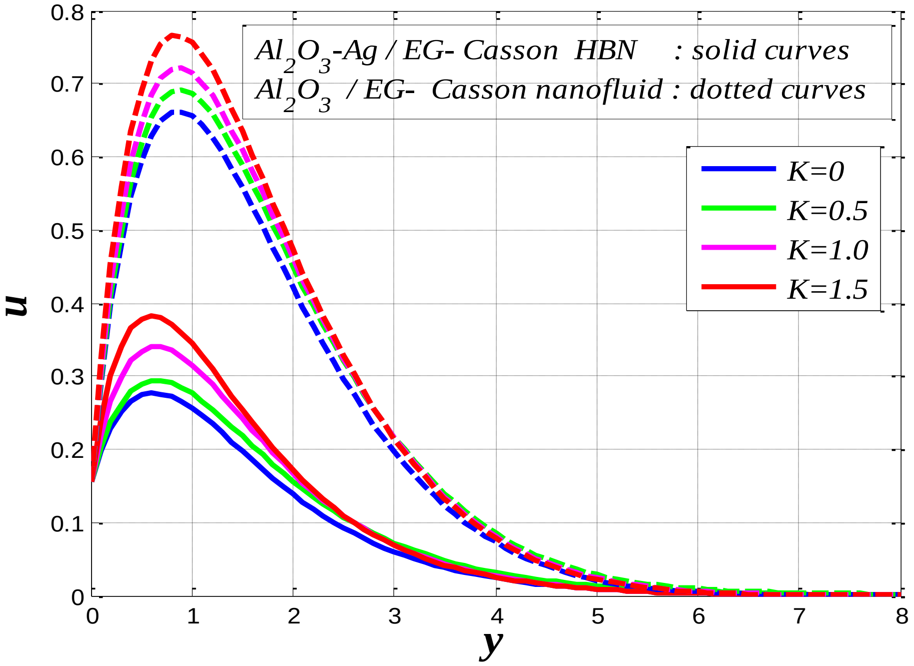

Fig. 16 Impact of electroosmosis parameter on axial velocity for fixed values of $Pr = 0.71;\ \phi_1 = 0.05;\ \phi_2 = 0.15; R = 0.5; t = 0.9; H = 0.5; Uhs = 1; k_1 = 0.5; Ta = 0.3; \beta = 1;\ a_0 = \frac{\pi}{2}; M = 0.4;\ Gr = 1.5$.

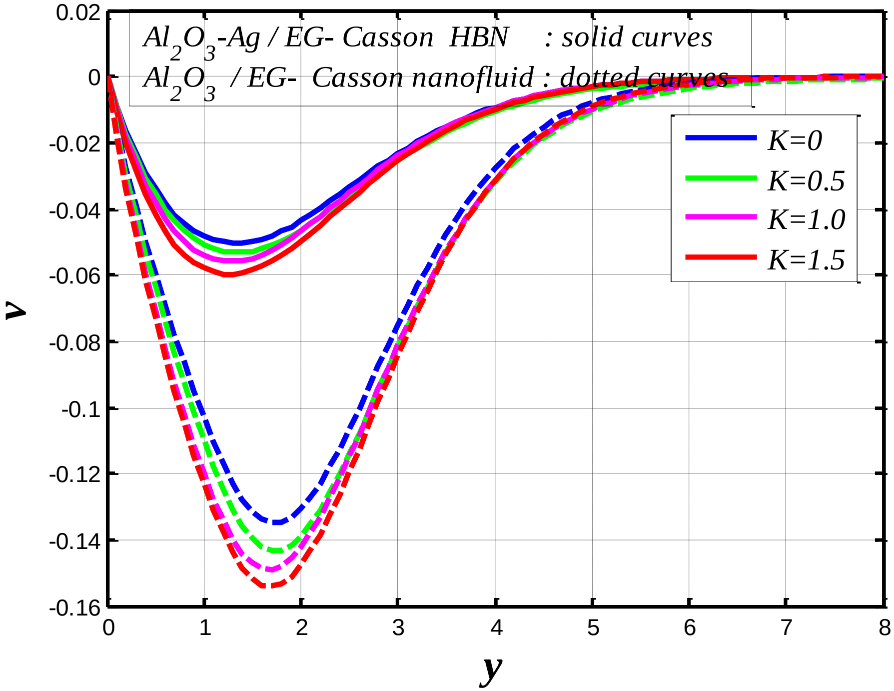

Fig. 17 Impact of electroosmosis parameter on transverse velocity for fixed values of $Pr = 0.71;\ \phi_1 = 0.05;\ \phi_2 = 0.15; R = 0.5; t = 0.9; H = 0.5; Uhs = 1; k_1 = 0.5; Ta = 0.3; \beta = \ 1;\ a_0 = \frac{\pi}{2}; M = 0.4;\ Gr = 1.5$.

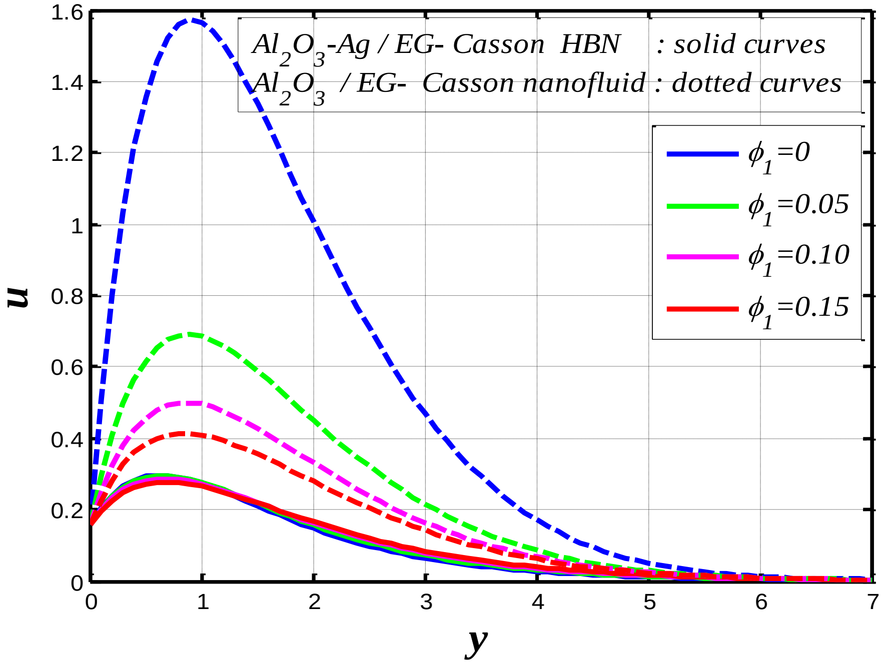

Fig. 18 Impact of Al_2O_3 nanoparticle volume fraction on axial velocity for fixed values of $Pr = 0.71;\ \ \phi_2 = 0.15; R = 0.5; t = 0.9; H = 0.5; Uhs = 1; k_1 = 0.5; Ta = 0.3; \beta = \ 1;\ K = 0.5;\ a_0 = \frac{\pi}{2}; M = 0.4;\ Gr = 1.5$.

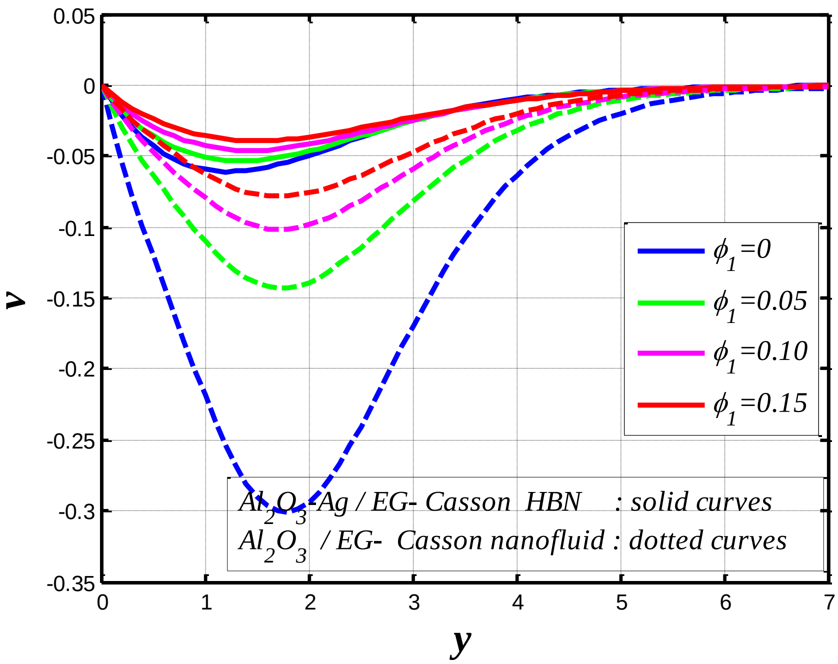

Fig. 19 Impact of Al_2O_3 nanoparticle volume fraction on transverse velocity velocity for fixed values of $Pr = 0.71;\ \phi_2 = 0.15; R = 0.5; t = 0.9; H = 0.5; Uhs = 1; k_1 = 0.5; Ta = 0.3; \beta = 1;\ K = 0.5;\ a_0 = \frac{\pi}{2}; M = 0.4;\ Gr = 1.5$.

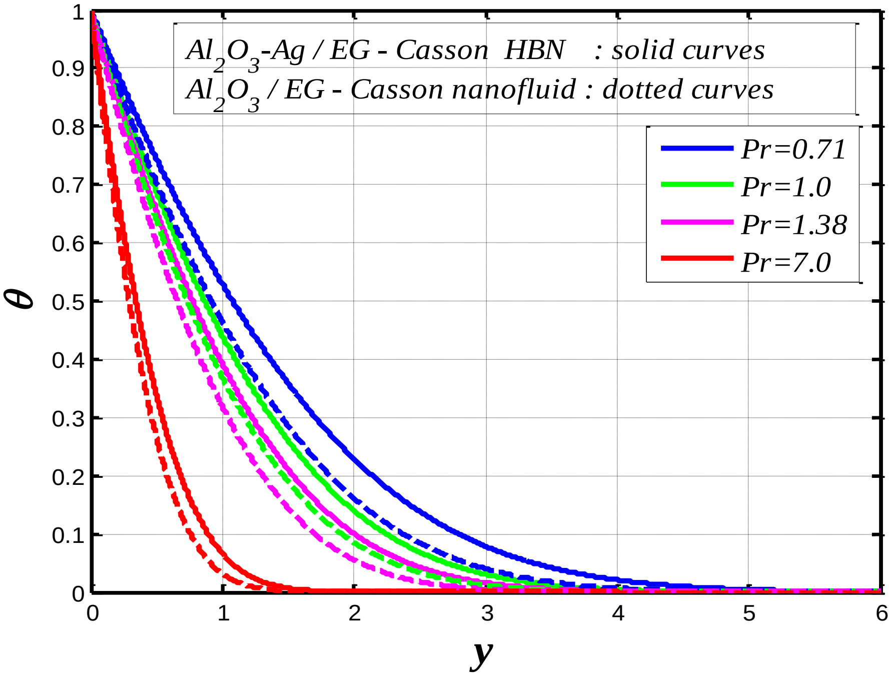

Fig. 20 Impact of Prandtl number on nanoparticle temperature profile velocity for fixed values of $\phi_1 = 0.05;\ \phi_2 = 0.15; R = 0.5; t = 0.8; H = 0.5;$

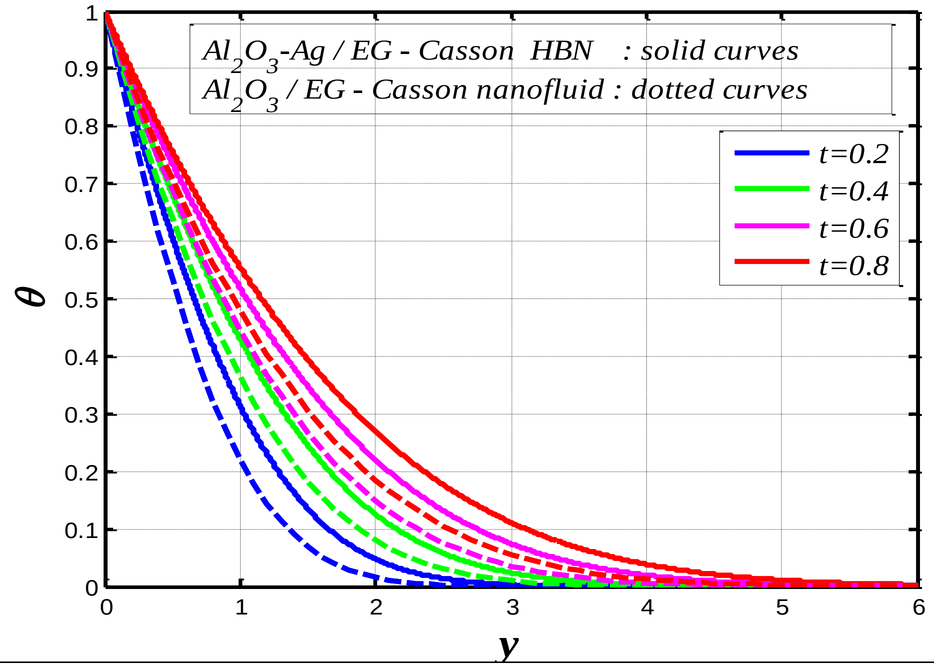

Fig. 21 Impact of time parameter on nanoparticle temperature profile for fixed values of $Pr = 0.71$; $\phi_2 = 0.05$; $\phi_2 = 0.15$; $R = 0.1$; $H = 0.5$

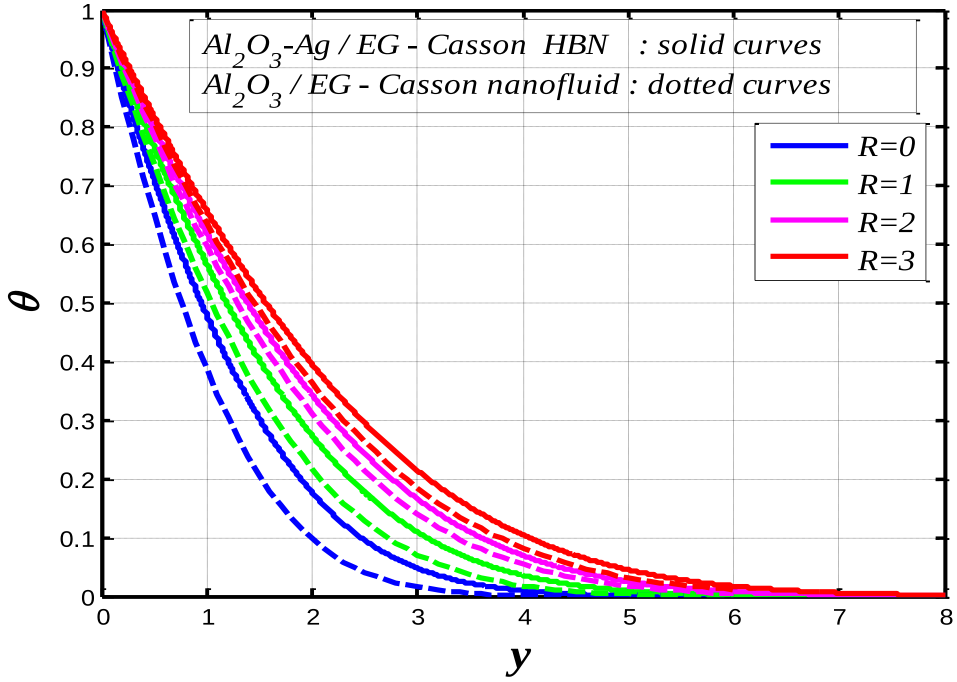

Fig. 22 Variation in nanoparticle temperature with thermal radiation parameter for fixed values of $Pr = 0.71$; $\phi_2 = 0.05$; $\phi_2 = 0.15$; $t = 0.5$; $H = 3$;

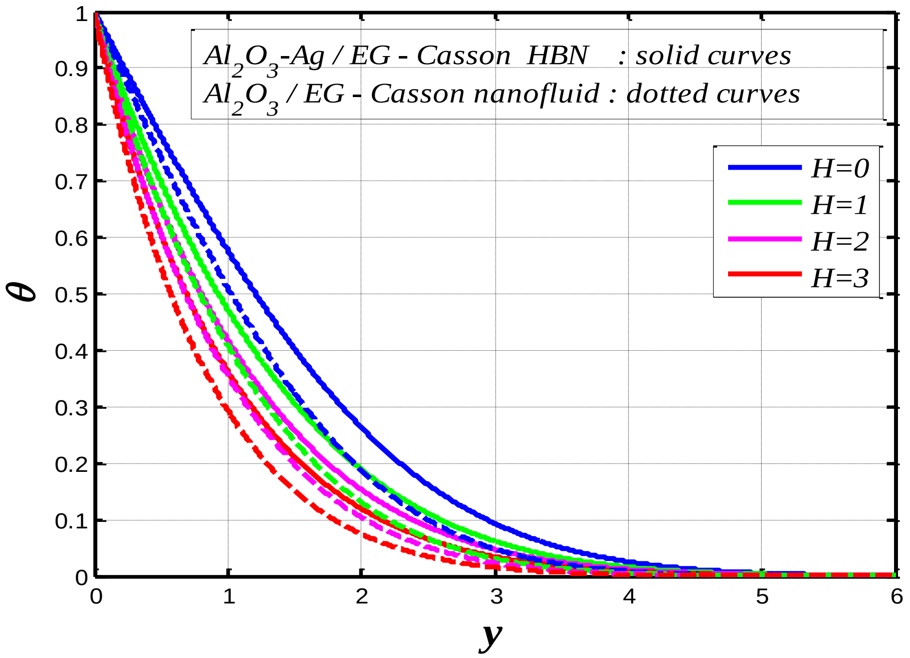

Fig. 23 Impact of heat generationparameter on nanoparticle temperature profile for fixed values of $Pr = 0.71;\ \phi_2 = 0.05;\ \phi_2 = 0.15; R = 0.5; t = 0.5;$

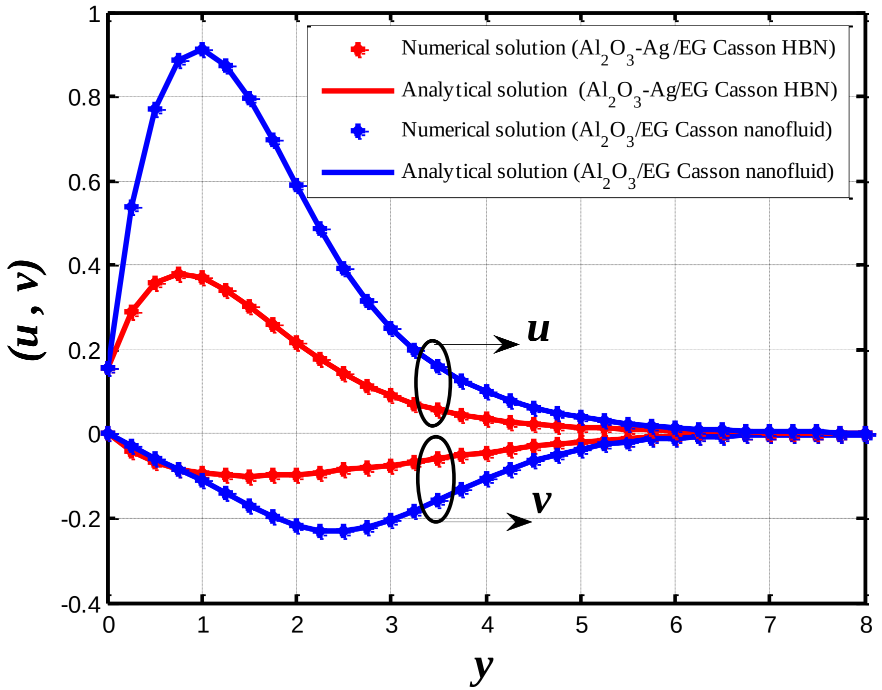

Fig. 24 Comparsion between the numerical solution with MATLAB pdepe command and analytical solution using theLaplace transform method (LTM) for fixed values of $Pr = 0.71;\ \phi_1 = 0.05;\ \phi_2 = 0.15; R = 0.5; t = 0.9; H = 0.5; Uhs = 1; k_1 = 0.5; Ta = 0.3; K = 0.5; a_0 = \frac{\pi}{2}; \beta = 1; Gr = 1.5;\ M = 0.4$.

NOMENCLATURE

ρ_{hnf}	*density of hybrid nanofluid* (kg/m^3)
$(\tilde{u}, \tilde{v})$	*dimensioanl axial and transverse velocity* (ms^{-1}) *in the direction of* $(\tilde{x}, \tilde{y})$
$\tilde{t}$	*dimensional time (s)*
β	*Casson fluid parameter*
$\tilde{\omega}$	*angular velocity*(s^{-1})
σ_{hnf}	*electrical conductivity (S/m)*
$\tilde{k}$	*porosity parameter(Darcy)*
$\tilde{\rho}_e$	*net charge number density*
$E_{\tilde{\chi}}$	*electric body force term*
$\tilde{T}$	*dimensional temperature (K)*
T_∞	*temperature of the fluid far away from the plate(K)*
π	*component of deformation rate,*
γ_{hnf}	*thermal expansion coefficient* (K^{-1})
μ_{hnf}	*dynamic viscosity* $(kg\, m^{-1} s^{-1})$
Q_0	*heat source/sink rate* (kg m^{-1}s^{-3})
C_p	*specific heat capacitance (J/kg.K)*
κ_{hnf}	*thermal conductivity(W/mK)*
$\tilde{q}_r$	*radiative heat flux* (kg s^{-3})
g	*acceleration due to gravity* (m s^{-2})
t	*dimensionless time*
z	*valence*
(n^-, n^+)	*number of anions and cations*
n_0	*mass ionic concentration* (m^{-3})
e	*electronic charge* $(\mathrm{kg}^{1/2}\mathrm{m}\Omega^{-1/2}\,\mathrm{sec}^{-1/2})$
σ^*	*Stefan-Boltzmann constant* $\left(Kg\, s^{-3} K^{-4}\right)$
k^*	*mean absorption coefficient* (m^{-1})
ε_{eff}	*relative permittivity of the vacuum* $\left(A^2 m^{-3}\,\mathrm{s}^4\, kg^{-1} = m^{-1}\,\mathrm{s}\,(\Omega hm)^{-1}\right)$
k_B	*Boltzmann constant* $(\mathrm{kgm}^2\mathrm{sec}^{-2}\mathrm{Kelvin}^{-1})$
T_v	*mean temperature (K)*
u_0	*initial velocity* (ms^{-1})
ϕ_1	*volume fraction of* Al_2O_3
ϕ_2	*silver nanoparticles*
P_y	*yield stress of the viscoplastic nanofluid*

$\tilde{a}_0$	*dimensional frequency parameter*
a_0	*dimensionless frequency parameter*
k_1	*porous (permeability) parameter*
θ	*nanoparticle temperature*
K	*electroosmosis parameter*
E	*potential function*
(u, v)	*dimensionless component of axial and transverse velocities of (x, y) direction*
Uhs	*electroosmotic velocity or Helmholtz-Smoluchowski velocity (HS velocity)*
Gr	*thermal Grashof number*
Ta	*Taylor number*
Pr	*Prandtl number*
R	*thermal radiation parameter*
H	*heat absorption/generation parameter*
Nu	*Nusselt number*
M	*Hartmann number*
k	*Permeability parameter (porous)*

Subscript

$(\ )_1$	Al_2O_3 *nanoparticles*
$(\ )_2$	*Ag nanoparticles*
$(\ )_{bf}$	*base fluid*

REFERENCES

1. Moreau, R.: Magnetohydrodynamics, Kluwer Academic Publishers (1990).

2. D.J. Griffiths, Introduction to Electrodynamics, Prentice Hall, 3rd Edition (1999).

3. L. Wang and J. Liu, Electromagnetic rotation of a liquid metal sphere or pool within a solution, Proc Roy Soc A: Math, Phys EngSci, 471, 2178 (2015). https://doi.org/10.1098/rspa.2015.0177

4. H. Chen et al., Experimental investigation on electroosmotic transport in cross/straight channel, 1st IEEE International Conference on Nano/Micro Engineered and Molecular Systems, Zhuhai, China 18-21 Jan (2006).

5. El-Genk, M.S. and Paramonov, D.V., An integrated model of the Topaz-II electromagnetic pump, Nuclear Technology, Vol. 108, No. 2, 1994, pp. 171-180.
6. Pascal Tixador. Magnetic levitation and MHD propulsion. Journal de Physique III, EDP Sciences, 4 (4), pp.581-593 (1994).
7. Shamshuddin MD, Siva Reddy Sheri and O Anwar Bég, Oscillatory dissipative conjugate heat and mass transfer in chemically reacting micropolar flow with wall couple stress: A finite element numerical study, Proc IMechE Part E: J Process Mechanical Engineering, 233 (1), 48-64 (2019).
8. Lang Yang, Jie Mao, Baolong Xiong, Numerical simulation of liquid metal MHD flows in a conducting rectangular duct with triangular strips, Fusion Engineering and Design, 163, 112152 (2021).
9. O. Anwar Bég, Tasveer A. Bég, I. Karim, M. S. Khan, M. M. Alam, M Ferdows, M. Shamshuddin, Numerical study of magneto-convective heat and mass transfer from inclined surface with Soret diffusion and heat generation effects: A model for ocean magnetohydrodynamic energy generator fluid dynamics, Chinese J. Physics, 60, 167-179 (2019).
10. Siva Reddy Sheri, O. Anwar Bég, P. Modugula and A. Kadir, Computation of transient radiative reactive thermo-solutal magneto-hydrodynamic convection in inclined MHD Hall generator flow with dissipation and cross diffusion, Computational Thermal Sciences, 11 (6) 541-563 (2019).
11. A.S. Hollinger and P.J.A. Kennis, Electrohydrodynamic-Jet Deposition of Pt-Based Fuel Cell Catalysts, ASME 2016 14th International Conference on Fuel Cell Science, Engineering and Technology/ASME 2016 Power Conference and the ASME 2016 10th

International Conference on Energy Sustainability, Charlotte, North Carolina, USA, June 23 (2016).

12. Nishihara M., Takashima K., Rich J. W., Adamovich I. V., Mach 5 bow shock control by a nanosecond pulse surface dielectric barrier discharges, Physics of Fluids, 50, 1-10 (2011).
13. S. Mandal et al., Drop deformation and emulsion rheology under the combined influence of uniform electric field and linear flow, Journal of Fluid Mechanics, 841 , 408 – 433 (2018).
14. M.H. Oddy et al., Electrokinetic instability micromixing, Anal. Chem. 73, 24, 5822–5832 (2001).
15. V K Narla, Dharmendra Tripathi, O. Anwar Bég and A Kadir, Modelling transient magnetohydrodynamic peristaltic pumping of electroconductive viscoelastic fluids through a deformable curved channel, Journal of Engineering Mathematics, 111, 127–143(2018).
16. M. M. Meighan et al., Bioanalytical separations using electric field gradient techniques, Electrophoresis, 30(5):852-65 (2009).
17. Bhandari, D. S., Tripathi, D. &Narla, V. K., Magnetohydrodynamics-based pumping flow model with propagative rhythmic membrane contraction. The European Physical Journal Plus, 135(11), 1-19 (2020).
18. D. Tripathi, Shashi Bhushan and O. Anwar Bég, Unsteady viscous flow driven by peristalsis and electrokinetics, Alexandria Eng. Journal (2017) (11 pages) .doi.org/10.1016/j.aej.2017.05.027
19. D. Tripathi, Abhilesh Borode, Ravinder Jhorar, O. Anwar Bég, Three-layered electro-osmosis modulated blood flow through a microchannel, European Journal of Mechanics / B Fluids, 72, 391-402 (2018).

20. Bianchi, F., Ferrigno, R. and Girault, H. H., Finite element simulation of an electroosmotic driven flow division at a T-junction of microscale dimensions, Analytical Chemistry, 72, 1987–1993 (2000).
21. N. Ali, S. Hussain, K. Ullah, O. Anwar Bég, Mathematical modelling of Ellis/Newtonian two-fluid electro-osmotic peristaltic pumping in an axisymmetric tube, European Physical Journal Plus, 134, 1-18 (2019).
22. Hsu, J. P., Kao, C. Y., Tseng, S. J. and Chen, C. J., Electrokinetic flow through an elliptical microchannel: effects of aspect ratio and electrical boundary conditions, Journal of Colloid Interface Science, 248, pp. 176–184 (2002).
23. Dharmendra Tripathi, Ashu Yadav, O. Anwar Bég and R. Kumar, Study of microvascular non-Newtonian blood flow modulated by electro-osmosis, Microvascular Research, 117, 28-36 (2018).
24. Tsao, H. K., Electroosmotic flow through an annulus, Journal of Colloid Interface Science, 225, pp. 247–250 (2000).
25. Dharmendra Tripathi, RavindraJhorar. O. Anwar Bég, Sachin Shaw, Electroosmosis modulated peristaltic biorheological flow through an asymmetric microchannel: mathematical model, Meccanica, 53, 2079–2090 (2018).
26. J. Liu et al., Design of a pulsatile DC electromagnetic blood pump for ECMO, Technology and Health Care, 25 (4) 809-814 (2017).
27. Tripathi, D., Jhorar, R., Bég, O. A., & Kadir, A. (2017). Electro-magneto-hydrodynamic peristaltic pumping of couple stress biofluids through a complex wavy micro-channel. Journal of Molecular Liquids, 236, 358-367.

28. Chakraborty, R., Dey, R., & Chakraborty, S. (2013). Thermal characteristics of electromagnetohydrodynamic flows in narrow channels with viscous dissipation and Joule heating under constant wall heat flux. International Journal of Heat and Mass Transfer, 67, 1151-1162.

29. Si, D., & Jian, Y. (2015). Electromagnetohydrodynamic (EMHD) micropump of Jeffrey fluids through two parallel microchannels with corrugated walls. Journal of Physics D: Applied Physics, 48(8), 085501.

30. Liu, Y., Jian, Y., & Tan, W. (2018). Entropy generation of electromagnetohydrodynamic (EMHD) flow in a curved rectangular microchannel. International Journal of Heat and Mass Transfer, 127, 901-913.

31. Reddy, P. D. S., Bandyopadhyay, D., Joo, S. W., Sharma, A., & Qian, S. (2011). Parametric study on instabilities in a two-layer electromagnetohydrodynamic channel flow confined between two parallel electrodes. Physical Review E, 83(3), 036313.

32. Santhosh Nallapu, Radhakrishnamacharya G, Chamkha Ali J. Flow of a Jeffrey fluid through a porous medium in narrow tubes. J Porous Media; 18:71–8 (2015).

33. O. Anwar Bég, J. Zueco, M. Norouzi, M. Davoodi, A. A. Joneidi, Assma F. Elsayed, Network and Nakamura tridiagonal computational simulation of electrically-conducting biopolymer micro-morphic transport phenomena, Computers in Biology and Medicine, 44, 44–56 (2014).

34. R. L. Batra and M. Eissa, Helical flow of a Sutterby model fluid, Polymer-Plastics Technology and Engineering, 33, 489-501 (1994).

35. M. O. Ullah, Mustapha Norzieha, S. Sharidan. Non-linear peristaltic flow of Walter's B fluid in an asymmetric channel with heat transfer and chemical reactions. ThermSci 18:1095–107 (2014).
36. Bhandari, D. S., Tripathi, D., &Narla, V. K. (2020). Pumping flow model for couple stress fluids with a propagative membrane contraction. International Journal of Mechanical Sciences, 188, 105949.
37. Khan I, Farhad A, Sharidan S. Exact solutions for unsteady MHD oscillatory flow of a Maxwell fluid in a porous medium. Z Naturforsch A, 68:635–45 (2013).
38. D. Tripathi, O. Anwar Bég and J. Curiel-Sosa, Homotopy semi-numerical simulation of peristaltic flow of generalized Oldroyd-B fluids with slip effects, Computer Methods in Biomechanics Biomedical Engineering, 17(4) 433-442 (2014).
39. N. Manzoor, O. Anwar Bég, K. Maqbool and S. Shaheen, Mathematical modelling of ciliary propulsion of an electrically conducting Johnson-Segalman physiological fluid in a channel with slip, Computer Methods in Biomechanics and Biomedical Engineering (2019). https://doi.org/10.1080/10255842.2019.1582033
40. N. Ali, Z. Asghar, M. Sajid, O. Anwar Bég, Biological interactions between Carreau fluid and micro-swimmers in a complex wavy canal with MHD effects, J. Brazilian Soc. Mech. Sci. Eng. 041:446 (2019)) DOI.ORG/10.1007/s40430-019-1953-y (13 pages).
41. Claudio L.A.Berli and María L. Olivares, Electrokinetic flow of non-Newtonian fluids in microchannels, Journal of Colloid and Interface Science, 320, 582-589 (2008).
42. Casson N. A flow equation for the pigment oil suspensions of the printing ink type. In: Rheology of disperse systems. New York: Pergamon; 1959. p. 84–102.

43. S. Charm and G. Kurland, Viscometry of human blood for shear rates of 0-100,000 sec−1, Nature, vol. 206, no. 4984, pp. 617–618, 1965.
44. G. W. S. Blair and D. C. Spanner, An Introduction to Biorheology, Elsevier Scientific, Oxford, UK, 1974.
45. J. Aroesty and J. F. Gross, Pulsatile flow in small blood vessels. I. Casson theory, Biorheology, vol. 9, no. 1, pp. 33–43, 1972.
46. A. Khalid, I. Khan, S. Shafie, Exact solutions for unsteady free convection flow of Casson fluid over an oscillating vertical plate with constant wall temperature, Abst. App. Anal., vol. 2015, Article ID 946350, 2015.
47. C. Sulochana, S.S. Payed, N. Sandeep, Non-Uniform heat source or sink effects on the flow of 3D Casson fluid in the presence of Soret and thermal radiation, Int. J. Eng. Res. Africa, Vol.20, pp. 112 – 129, 2015.
48. C.S.K. Raju, N. Sandeep, V. Sugunamma, M.J. Babu, J.V. Ramana Reddy, Heat and mass transfer on magneto hydrodynamic casson fluid over an exponentially permeable stretching surface, Eng. Sci. Tech., Int. J., 19 (2016) 45 -52.
49. N. S. Akbar, D. Tripathi, O. Anwar Bég, Z. H. Khan, MHD dissipative flow and heat transfer of Casson fluids due to metachronal wave propulsion of beating cilia with thermal and velocity slip effects under an oblique magnetic field, ActaAstronautica, 128, 1-12 (2016).
50. S.K. Das, Nanofluids: Science and Technology, CRC Press, Florida (2007).
51. MD. Shamshuddin, S.R. Mishra, O. Anwar Bég, T.A. Bég and Ali Kadir, Computation of radiative Marangoni (thermocapillary) magnetohydrodynamic convection in Cu-water

based nanofluid flow from a disk in porous media: smart coating simulation, Heat Transfer (2020). DOI: 10.1002/htj.21963 (20 pages)

52. J.C. Umavathi and O. Anwar Bég, Modelling the onset of thermosolutal convective instability in a non-Newtonian nanofluid-saturated porous medium layer, Chinese J. Physics, 68, 147–167 (2020).
53. Ankita Dubey, B. Vasu, O. Anwar Bég and Rama S R Gorla, Numerical simulation of two-fluid non-Newtonian nano-hemodynamics through a diseased artery with a stenosis and aneurysm, Computer Methods in Biomechanics and Biomedical Engineering (2019). DOI: 10.1080/10255842.2020.1729755 (28 pages)
54. D. Tripathi, Noreen Akbar, O. Anwar Bég, Transient peristaltic diffusion of nanofluids: A model for micropumps in medical engineering, J. Hydrodynamics, 30(6): 774-781 (2018).
55. K. Vajravelu, K.V. Prasad, Jinho Lee, Changhoon Lee, I. Pop, Robert A. Van Gorder, Convective heat transfer in the flow of viscous Ag-water and Cu- water nanofluids over a stretching surface, Int. J. Therm. Sci. 50 (2011) 843–851.
56. SireetornKuharat, O. Anwar Bég, Ali Kadir, B. Vasu, Tasveer A. Bég and W.S. Jouri, Computation of gold-water nanofluid natural convection in a three-dimensional tilted prismatic solar enclosure with aspect ratio and volume fraction effects, Nanoscience and Technology- An International Journal, 11 (2), 141-167 (2020).
57. K Ramesh, M Gnaneswara Reddy, M Devakar, Biomechanical study of magnetohydrodynamic Prandtl nanofluid in a physiological vessel with thermal radiation and chemical reaction, Proc. IMechE-Part N: J Nanoengineering, Nanomaterials and Nano-systems, 232, 95-108 (2018).

58. M. Aneja, Sapna Sharma, S. Kuharat and O. Anwar Bég, Computation of electroconductive gyrotactic bioconvection under nonuniform magnetic field: Simulation of smart bio-nanopolymer coatings for solar energy, Int. J. Modern Physics B, 33, 2050028 (22 pages). (2020)
59. M. Fatima, A. Sohail, KhushBakhatAkram, L. Sherin, SaadIhsan Butt, M. Abid and O. Anwar Bég, Biomechanics of superparamagnetic nanoparticles for laser hyperthermia, Biomedical Engineering: Applications, Basis and Communications, 32, No. 1 (2020) 2050007 (11 pages) DOI: 10.4015/ S1016237220500076
60. H. ThameemBasha, R. Sivaraj, V. Ramachandra Prasad and O. Anwar Bég, Computation of non-similar flow of a magnetic pseudoplastic nanofluid over a circular cylinder with variable thermophysical properties and radiative flux, Int. J. Num. Meth. Heat Fluid Flow (2020). 0961-5539 DOI 10.1108/HFF-04-2020-0236 (45 pages)
61. B. Vasu, A. Dubey and O. Anwar Bég, Finite element analysis of non-Newtonian magneto-hemodynamic flow conveying nanoparticles through a stenosed coronary artery, Heat Transfer-Asian Research (2019). DOI: 10.1002/htj.21598 (34 pages)
62. O. Anwar Bég, Ayesha Sohail, T.A. Bég and A. Kadir, B-spline collocation simulation of nonlinear transient magnetic nano-bio-tribological squeeze film flow, J. Mechanics in Medicine and Biology, 18, 1850007.1- 1850007.20 (20 pages) (2018).
63. Dharmendra Tripathi, Ashish Sharma and O. Anwar Bég, Joule heating and buoyancy effects in electro-osmotic peristaltic transport of nanofluids through a microchannel with complex wave propagation, Advanced Powder Technology, 29, 639-653 (2018).
64. G.P. Zhao et al., Electromagnetohydrodynamic flow and heat transfer of nanofluid in a parallel plate microchannel, J Mechanics, 33, 115-124 (2017).

65. J. Prakash, E.P. Siva, D. Tripathi and O. Anwar Bég, Thermal slip and radiative heat transfer effects on electro-osmotic magneto-nanoliquid peristaltic propulsion through a microchannel, Heat Transfer-Asian Research (2019). 27 pages. DOI: 10.1002/htj.21522
66. A.M. Rashad, A.J. Chamkha, M.A. Ismael, T. Salah, Magnetohydrodynamics natural convection in a triangular cavity filled with a Cu-Al2O3/water hybrid nanofluid with localized heating from below and internal heat generation, ASME Journal of Heat Transfer, 140(7) (2018) 072502.
67. L.A. Lund, Z. Omar, I. Khan, E.S.M. Sherif, Dual solutions and stability analysis of a hybrid nanofluid over a stretching/shrinking sheet executing MHD Flow. Symmetry 2020, 12, 276.
68. T. Hayat, S. Nadeem, Heat transfer enhancement with Ag-CuO/water hybrid nanofluid. Results Phys. 2017, 7, 2317–2324.
69. J. Prakash, D. Tripathi, O. Anwar Bég, Comparative study of hybrid nanofluid performance in microchannel slip flow induced by electroosmosis and peristalsis, Applied Nanoscience (2020). (14 pages). doi.org/10.1007/s13204-020-01286-1.